

INTRACLUSTER LIGHT IN NEARBY GALAXY CLUSTERS: RELATIONSHIP TO THE HALOS OF BRIGHTEST CLUSTER GALAXIES

ANTHONY H. GONZALEZ¹

Department of Astronomy, University of Florida, Gainesville, FL 32611

AND

ANN I. ZABLUDOFF AND DENNIS ZARITSKY

Steward Observatory, University of Arizona, 933 North Cherry Avenue, Tucson, AZ 85721

Submitted to The Astrophysical Journal

ABSTRACT

We present a detailed analysis of the surface brightness distribution of the brightest cluster galaxy (BCG) in each of 24 galaxy clusters at $0.03 < z < 0.13$. We use two-dimensional profile fitting to model the surface brightness out to $r = 300$ kpc for each BCG, comparing $r^{1/4}$, $r^{1/n}$, and double $r^{1/4}$ models. We obtain statistically superior fits using a two component model consisting of a pair of $r^{1/4}$ profiles with independent scale lengths, ellipticities, and orientations. The two component model can simply reproduce the observed position angle and ellipticity gradients, which cannot generally be explained purely by triaxiality. The inner component of our two component model has properties similar to a typical massive elliptical galaxy and is clearly associated with the BCG. The outer component is 10-40 times larger in scale, has ~ 10 times the total luminosity of the inner component, and exhibits a steeper $< \mu > -r_e$ relation than that of the elliptical fundamental plane. We interpret this outer component as a population of intracluster stars tracing the cluster potential. The two components are strongly aligned ($|\Delta\theta| < 10^\circ$) in roughly 40% of the clusters. When they are not aligned, the components tend toward high degrees of misalignment, suggesting that accretion of infalling material may change the orientation of some BCGs for a time. The extent of the outer component and its similar elongation to published cluster galaxy distributions indicates that the evolution of the intracluster light is tied to the cluster as a whole rather than to the BCG.

Subject headings: galaxies: clusters: general — galaxies:cD, formation, evolution, fundamental parameters

1. INTRODUCTION

One of the most distinctive characteristics of brightest cluster galaxies (BCGs) is that many exhibit shallower extended surface brightness profiles than their lower mass elliptical counterparts. This trait was first recognized by Mathews, Morgan & Schmidt (1964), who observed that some BCGs emit more light at large radii than would be expected for an $r^{1/4}$ profile. This excess emission, which is often lumped into the term “cD” envelope,² was confirmed by Oemler (1973, 1976) and Schombert (1986, 1987, 1988) in a subset of BCGs.

What is the nature of this excess luminosity at large radii? Schombert, who considered two-component models when fitting surface brightness profiles to $r \sim 200 - 1500$ kpc, argued that the extended light is physically distinct from the central galaxy. In this picture, the excess light component is thought to arise from a population of intracluster stars produced by the tidal stripping and disruption of cluster galaxies (c.f. Gallagher & Ostriker 1972; Dressler 1979; Richstone & Malamuth 1983; Miller 1983; Malamuth & Richstone 1984; Merritt 1984; Sommer-Larsen, Romeo, & Portinari 2004; Murante et al. 2004; Willman et al. 2004). Simulations predict that this intracluster light (ICL) is comprised of old stars that are dynamically distinct from the stars in the BCG (Sommer-Larsen, Romeo, & Portinari 2004; Murante et al. 2004) and that production of intracluster stars is an ongoing

process (Willman et al. 2004). If correct, this model implies that the properties of the ICL, including its fractional contribution to the total cluster luminosity and its spatial distribution, are sensitive probes of the physical processes driving cluster formation and the evolution of cluster galaxies.

Subsequent studies using CCD detectors have generally lacked either the statistics or the radial coverage required to test this interpretation. Moreover, most recent measurements of individual BCG profiles out to large radii ($r \gtrsim 200$ kpc) have failed to detect a second component. With the exception of Feldmeier et al. (2002), these studies find profiles that are roughly consistent with a pure $r^{1/4}$ law (Uson, Bough, & Kuhn 1990, 1991; Scheick & Kuhn 1994; Gonzalez et al. 2000). With this program we aim to utilize a large sample of BCGs to constrain the ubiquity of the outer component and to quantify the properties of this component if it exists.

Our work extends beyond previous studies in several ways. First, by utilizing highly uniform drift-scan data we provide the first observations that recover the profiles for a statistical sample of BCGs to large radii using modern CCD photometry. Specifically, we present the surface brightness profiles to $r \gtrsim 300$ kpc for 24 BCGs. Second, scanning provides long, contiguous images obtained with the same CCD. The importance of a precise and accurate sky level is paramount in this type of study, and the geometry of drift-scans facilitates this endeavor. Third, while previous studies typically either azimuthally average or model the surface brightness profile along the semi-major axis, we employ full two-dimensional modelling. This approach enables us to model ellipticity or position angle gradients that may be present and to simulta-

Electronic address: anthony@astro.ufl.edu

¹ NSF Astronomy and Astrophysics Postdoctoral Fellow

² This emission is differentiated into categories by some experts (see Schombert 1986).

neously model multiple objects. The latter minimizes the impact on the profile of other galaxies projected near the center of the BCG.

The organization of this paper is as follows. In §2 we discuss the data and preliminary reductions. In §3 we describe the modelling of the galaxies and present the resulting profiles. In §4 we find that two-component fits provide better fits to the profiles than one-component models, compare the relative properties (luminosity, effective radius, ellipticity, position angle, centroid) of the two components, discuss the fundamental plane for both components, and consider how one-component fits impact determination of the BCG total magnitudes and fundamental plane. We assess the robustness of the derived structural parameters in the Appendix. Finally, we summarize our conclusions in §5. Throughout the paper we assume a cosmology with $H_0 = 70 \text{ km s}^{-1} \text{ Mpc}^{-1}$, $\Omega = 0.3$, and $\Lambda = 0.7$.

Our results provide important tests for the new generation of cosmological cluster simulations that have both the force resolution and complexity to generate intracluster stars (Sommer-Larsen, Romeo, & Portinari 2004; Murante et al. 2004; Willman et al. 2004) and that are beginning to make predictions for the properties of this population.

2. DATA AND REDUCTIONS

2.1. Sample Definition

We observed a total of 30 clusters spanning a range of velocity dispersions and Bautz-Morgan types (Bautz & Morgan 1970). Our sample consists of nearby clusters (published redshifts $0.08 < z < 0.12$) that contain BCGs with position angles within 45 degrees of the east-west axis (our drift scan direction). In this paper we focus on the 24 clusters with a single, dominant BCG that show no evidence of an ongoing merger. We note that Bautz-Morgan type III clusters are underrepresented in the full sample and that errors in the published redshifts yield a wider actual redshift range ($0.03 < z < 0.13$).

2.2. Data

We obtained drift scan data during four separate runs on the Las Campanas 1m Swope telescope between 1995 and 2000 (Table 1). Conditions were photometric during all runs, with the data from 2000 having the darkest sky and best seeing. All imaging was obtained in Gunn i using the Great Circle Camera (Zaritsky, Schectman, & Bredthauer 1996), and the photometry is calibrated to Cousins I using Landolt standards. Individual drift scans are 2048×10000 pixels with a plate scale of $0.7'' \text{ pixel}^{-1}$, except for the scans of Abell 1651, which are 13000 pixels long. Exposure times per scan vary depending upon the declination of the target, ranging from 95-133 seconds, with seven scans obtained for each target when possible. Observational details for each field, including total exposure time and seeing, are listed in Table 1. For the 24 clusters that are the focus of this paper we also include the Two Micron All Sky Survey (2MASS) Extended Source Catalog designation for the brightest cluster galaxy.

2.3. Reductions

The two factors that typically limit photometric measurements of low surface brightness features are variations in the detector response (i.e. flatness) and variations in the sky flux. Minimizing residual variations from both sources is critical for this program, as brightest cluster galaxies are expected to have $\mu_I \approx 26 \text{ mag arcsec}^{-2}$ at $r = 300 \text{ kpc}$. To reliably

model the profiles out to this radius, we require that this surface brightness exceed the 3σ systematic uncertainty in the sky level.

2.3.1. Flatfielding

The basic reduction procedure is similar in form to that described by Gonzalez et al. (2000). With drift-scan imaging, pixel-to-pixel variation is mitigated because data are clocked across the chip, and so sensitivity variations are a concern only perpendicular to the readout direction (at a level of $\sim 2\%$ in our raw data). After subtracting the bias, we use the scans to generate a one-dimensional flatfield, using sigma-clipped averaging to compute the sensitivity for each column. The accuracy of this initial flatfield is limited by both contamination from astronomical objects and temporal sky variations along the direction of readout.

We generate a second-pass flatness correction by masking objects and modelling the sky variations (details are given in the discussion of sky subtraction below). This improved flatfield is then applied to the original bias-subtracted images. We generate a single flatfield for each of the 1995 and 1999 observing runs, while for the 2000 run we have sufficient data to divide the run into three two-night subsets and generate an individual flatfield for each subset. The difference among these flatfields reflects the remaining uncorrected sensitivity variations. The rms difference between the second and third subsets of the 2000 data is 0.05%, with no detectable systematic variation. The flatfield from the first two nights exhibits a roughly linear systematic variation across the detector relative to the other subsets at the level of $\pm 0.17\%$, with an rms difference of 0.11%. We conclude that the residual flatness variations for a single scan in our data are $\lesssim 0.20\%$ (or $\mu_I \approx 26.4 \text{ mag arcsec}^{-2}$), with column-to-column rms variations $\approx 0.05\%$ ($\mu_I \approx 27.9 \text{ mag arcsec}^{-2}$). Residual variations are further mitigated by coadding the scans, and any remaining gradients (such as the linear difference between flatfields noted above) are muted further by the two-dimensional sky subtraction procedure described below.

2.3.2. Subtraction of Sky Variations: First Pass

The mean sky level typically changes by $\sim 3\%$ during single scan. To correct for this temporal variability, we first mask all objects in a scan to prevent them from biasing our model of the variation. We create a binary mask using segmentation images output by SExtractor 2.3 (Bertin & Arnouts 1996), excluding all pixels within the detection and buffer regions around each object. For objects with an area in excess of 250 sq. arcsec (primarily saturated stars), the buffer region consists of pixels within $150''$ of the object detection region. For smaller objects the buffer radius is either $50''$ (for those objects with area $> 25 \text{ sq. arcsec}$) or $5''$ (for those with area $< 25 \text{ sq. arcsec}$). As an added precaution, the entire region within $350''$ of the BCG is masked.

We then model sky variation along the scan with a five segment cubic spline. Subtraction of this model provides a first-pass removal of the large-scale temporal variations, which is a necessary prerequisite for co-adding. A more precise, two-dimensional modeling of the sky is performed at a later stage.

2.3.3. PSF Modelling

Following bias subtraction, flatfielding, and the first-pass sky subtraction, we register and average the scans to generate a single image for each cluster. A key concern at this stage

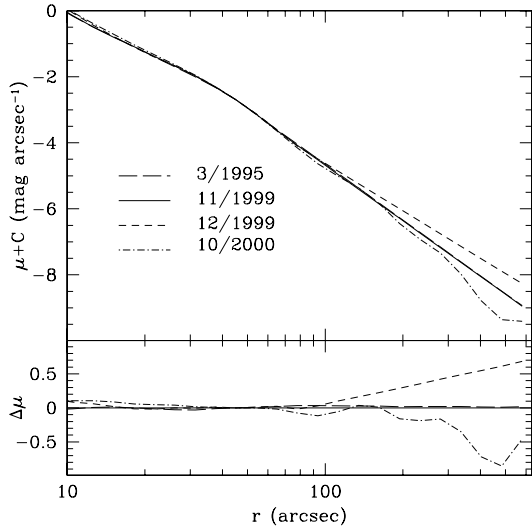


FIG. 1. — *Top*: Empirical model PSFs of saturated stars generated for each observing run, normalized to the same surface brightness at $50''$. The PSF for the March 1995 run is the least well determined, being constructed only from stars in the field of Abell 1651. We only plot $r > 10''$, where the profiles are independent of the mean seeing during the run. *Bottom*: Differences in the PSFs relative to the November 1999 run. The PSFs for the different runs agree to within roughly 30% out to $200''$.

is that the point spread function (PSF) of a bright, saturated star can introduce appreciable gradients in the sky level even at distances of several arcminutes. To minimize the impact of these stars on our photometry, we construct an azimuthally averaged model of the PSF out to $r = 1000$ pixels ($700''$). A single model is generated for each observing run via a luminosity weighted combination of all stars with $m_I \lesssim 12.2$ in images from that run, masking nearby objects and the saturated cores. The resulting PSF models are shown in Figure 1, normalized to have the same surface brightness at $50''$ radius. The PSF for the 1995 observing run is the least well constrained because it is generated using only stars from the field of Abell 1651. Nonetheless, all profiles agree to within $\sim 30\%$ out to $200''$, and the difference between profiles at $700''$ is not a dominant source of uncertainty in recovering the profile of the BCG unless a star with $m_I \lesssim 7$ lies within this distance. Abell 2376 and Abell 3809 are the only clusters in our sample with such a luminous nearby star, while for Abell 2405 a bright star lies just outside this radius.

2.3.4. Subtraction of Sky Variations: Second Pass

After accounting for the PSFs of bright stars, we proceed with a second pass to model the sky. The remaining large-scale gradients in the sky level may arise from both instrumental (uneven illumination) and astrophysical (dust emission) sources. We construct a background map via wavelet decomposition of the input image using the algorithm *wvdecomp* (Vikhlinin et al. 1998). We use an *à trous* wavelet transform to detect all structures with $> 2\sigma$ significance on scales of $2^0 - 2^9$ of $0.7'' - 358''$; see Starck & Murtagh 1994 and references therein for a detailed description of the *à trous* transform). We subtract these structures from the input image and then generate the background map by convolving the residual image with a kernel of scale 2^{10} pixels ($716''$). This scale is larger than the region within which the BCG profiles are modelled (typically $r \lesssim 250''$). We find no evidence

of oversubtraction in the region of the BCG at the level of $\mu = 27.3$ mag arcsec $^{-2}$ in stacked background images. The rms amplitude of the variations removed by subtraction of the background maps is equivalent to $\mu \simeq 26.8$ mag arcsec $^{-2}$.

Figure 2 illustrates the impact of PSF subtraction and wavelet removal of large scale gradients. The three masked images are shown at the same contrast and are Gaussian smoothed to enhance low surface brightness features.

3. MODELLING THE SURFACE BRIGHTNESS PROFILES

We model the brightest cluster galaxy surface brightness profiles using GALFIT, a two-dimensional galaxy-fitting program (Peng et al. 2002) that has several advantages for our work. First, it permits simultaneous modelling of multiple components. This feature enables us to model galaxies near the center of the BCG that could otherwise bias the derived profiles, to model systems with multiple dominant galaxies (in a subsequent study), and to model the BCGs themselves with multiple components. Second, because we fit the two-dimensional luminosity distribution rather than the surface brightness profile along the major axis, the χ^2 of the fit is directly sensitive to variations in the position angle and ellipticity with radius — unlike many previous studies. The gradients provide important leverage in discerning whether two component models for BCGs (e.g., Schombert 1986, 1988; Porter, Schneider, & Hoessel 1991) are superior to single component Sérsic and $r^{1/4}$ models. Finally, the program generates an image of the best-fit model, from which we calculate the model's radial profile using the same masking as used for the data. This radial profile is valuable both for visualization and comparison with previous studies.

There are five critical inputs to GALFIT, aside from the image itself, that warrant detailed discussion. These inputs are the stellar PSF, the image mask, the noise map, the mean sky level, and the parametric model for the surface brightness distribution. Each is discussed below, and the sensitivity of the results to the PSF, masking, and sky level are explored in the Appendix.

3.1. PSF

GALFIT requires a representation of the stellar PSF for its convolution with the galaxy model. We derive the PSF using the IRAF implementation of DAOPHOT II (Stetson 1987). A Moffat model with first order residual variations is generated for each image using the 150 brightest unsaturated stars.

3.2. Masks

Masks are generated using the procedure described in §2. A key difference is that here we do not automatically mask any objects within $20''$ of the center of the BCG. We visually inspect the images, manually masking these objects when possible and leaving them unmasked for modelling when necessary. We adopt the latter option only when part of the object lies within $\sim 5''$ of the BCG. Two clusters, Abell 2969 and Abell 3705 require special attention. In Abell 2969 two galaxies overlapping the BCG were modelled, while in Abell 3705 a single large, bright galaxy $2'$ away was modelled to minimize its impact upon the BCG profile at large radii.

For each BCG, we also exclude all pixels outside a circular aperture of physical radius 300 kpc. We choose a fixed physical radius to facilitate comparison of the profiles, and choose 300 kpc because this is roughly the distance at which the surface brightness along the semi-major axis is comparable to the

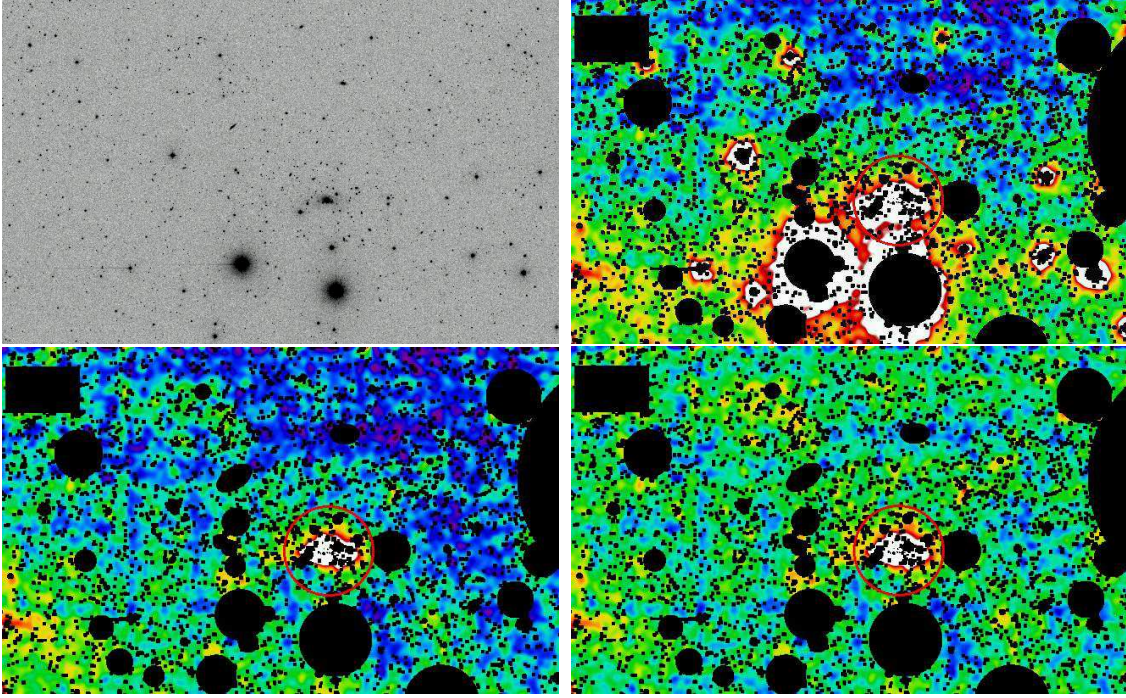


FIG. 2.— Series of images of Abell 0122 illustrating the impact of PSF subtraction and wavelet removal on the level of sky variation. The size of the region shown is $30' \times 19'$. The top left image is the data immediately after co-adding, with the saturation level corresponding to $\mu = 21.8$ mag arcsec $^{-2}$. Subsequent images are Gaussian smoothed to enhance the visibility of low surface brightness features and are each displayed with the same contrast. The saturation level in these images corresponds to $\mu = 25.8$ mag arcsec $^{-2}$. We mask objects other than the BCG, which is marked by an overlaid circle of radius 300 kpc (the size of the fitting region in §3). The upper right image, like the upper left panel, is constructed from the coadded individual scans. Significant excess flux is visible along the perimeters of stellar masks. The lower left panel demonstrates the improvement achieved with the PSF subtraction of saturated stars. Finally, the lower right panel demonstrates the improvement achieved, particularly in the uniformity of the background on large scales, by subtracting the wavelet background map.

5σ sky level uncertainty for most BCGs in our sample. For a typical BCG, $\sim 25 - 45\%$ of pixels within this physical aperture are masked. In only three cases does the masking exceed 50% of the pixels within this radius: Abell 2376, Abell 2405, and Abell 3705, with $\sim 55\%$ of pixels masked for each. For Abell 2376 and Abell 2405 the increased masking is due to a nearby bright star; for Abell 3705 the cluster simply lies in a region of high stellar density.

3.3. Noise maps

Noise maps are constructed directly from the data, which has zero mean sky due to previous processing. Objects are initially masked and the DIMSUM³ routine *iterstat* is used to directly compute the background rms noise level. Assuming Poisson statistics, we add the equivalent sky level to the image and take the square root to generate a noise map, which is then smoothed with a 2 pixel FWHM Gaussian. Smoothing provides a more robust measure of the noise level, and use of a smoothing scale comparable to the seeing minimizes spatial degradation of the noise map. While these noise maps yield model fits that are good in absolute terms (reduced $\chi^2 \simeq 1$; §4), because these noise maps are approximate we only draw conclusions from the relative χ^2 values derived for the different models.

3.4. Sky Level

The background level is a critical input because systematic error in the sky will dominate the profile at large radii. We use

GALFIT to determine the sky level, utilizing the same noise maps and masks as for the profile fitting. The sky level is measured within circular annuli of radii $r = 600 - 750$ kpc centered on the BCG. The extrapolated flux level of the central galaxy at these radii is more than 3 mag fainter than it is at 300 kpc (or equivalently $< 7\%$ as bright), which is 2-3 times less than our 1σ sky level uncertainty (see below), and hence negligibly impacts our estimate of the sky level.

We use the ensemble properties of our sample to quantify the uncertainty in the derived mean sky levels. The measured dispersion among the mean sky levels observed for different galaxies (σ_{obs}) has two sources: true differences in the global mean sky levels of different images (σ_g) and our measurement uncertainty within the background annuli (σ_m). If we assume that these contributions add in quadrature, then $\sigma_m^2 = \sigma_{obs}^2 - \sigma_g^2$. To estimate σ_g we measure the global sky level over the entire image (excluding the BCG region) for each cluster and then compute the dispersion. We then measure the mean sky level within the background annulus for each BCG and compute σ_{obs} . In both cases we use GALFIT to determine the mean sky level, and together these data enable us to derive σ_m , the 1σ uncertainty in the sky level. For a typical galaxy in our sample this 1σ uncertainty corresponds to $\mu \simeq 28.4$ mag arcsec $^{-2}$.⁴ In one case, Abell 2376, we increase our estimate of the sky uncertainty by a factor of two to account for the impact of a proximate bright star.

3.5. Input Models

³ DIMSUM is the Deep Infrared Mosaicing Software package developed by Peter Eisenhardt, Mark Dickinson, Adam Stanford, and John Ward.

⁴ The precise value varies depending on the photometric zeropoint of the field, because the calculation is performed using uncalibrated counts.

We test three different functional forms for the BCG surface brightness distribution. Two of these are single component deVaucouleurs ($r^{1/4}$) and Sérsic ($r^{1/n}$) models, while the third, in the spirit of Schombert (1988), is a two component model consisting of a pair of $r^{1/4}$ profiles with independent parameters. We will refer to the latter model as the 2-deV model henceforth. The $r^{1/n}$ model has one more degree of freedom (dof) than the $r^{1/4}$ model, while the second component in the 2-deV model adds six dof relative to the single $r^{1/4}$ model ($x, y, \mu_e, r_e, \theta, \epsilon$). For each functional model we run GALFIT with a series of different initial parameters to ensure convergence to the global minimum for each model, and iterate upon the solution until $\Delta\chi^2 < 10^{-3}$.

4. RESULTS AND DISCUSSION

4.1. Evidence for Two Components

The optimal parameters for each model and the $\Delta\chi^2$ values between different models are presented in Tables 2–4. In these Tables we include both the statistical parameter uncertainties from GALFIT and, in parentheses, the uncertainties corresponding to 1σ changes in the sky level (see §3.4 and the Appendix). To illustrate the quality of the models, we also present one-dimensional profiles extracted using the IRAF task *ellipse*. In Figure 3 we present surface brightness profiles along the semi-major axis, and in Figure 4 we show the residuals relative to the 2-deV model. In both figures we employ the same masking and elliptical apertures for the data and models to enable direct comparison.⁵ The model images output by GALFIT include convolution with the input PSF, and hence comparison to the data is valid over the entire radial range shown. In Figure 4 we overlay shaded regions corresponding to the 1σ systematic sky level uncertainty (§3.4A.1) to clarify the significance of deviations between the data and models.

Figures 5 and 6 show the ellipticities and position angles derived for both the data and best-fit models. While the single component models have fixed values for both quantities, there are gradients visible in the Figures for these models because we have folded into the profiles several additional factors to enable direct comparison with the data. First, masking of galaxies near the center of the BCG can lead to variations in both quantities. We use the same masking for both the data and models to ensure a fair comparison. Second, seeing acts to decrease the central ellipticity and can cause position angle changes if the ellipticity is small. The models are convolved with the PSF from the image and so exhibit the same decrease as the data. Third, in some instances we found it necessary to model rather than mask secondary galaxies near the center of the BCG, which are listed in the caption for Figure 5. The flux from these galaxies is included in the plotted profiles for both the data and models. Abell 2400 is a good example of the impact that such a companion can have on the central profile. Together the above factors explain the gradients seen in the single component models; yet, even including these factors, these models cannot reproduce the ellipticity and position angle variations observed in some of the BCGs.

⁵ A potential concern is that the lack of ellipticity and PA gradients for the Sérsic and $r^{1/4}$ models could bias the residuals shown in Figure 4. We have performed tests to assess the importance of this bias, and find that the effect is negligible.

4.1.1. Sérsic versus $r^{1/4}$

Our data demonstrate that the $r^{1/n}$ profile provides a dramatic improvement relative to the $r^{1/4}$ profile. The additional degree of freedom decreases χ^2 by an average of 3649 (Table 3), and substantially improves the fit at large radii (Figures 3–4). In only two cases is the decrease in $\Delta\chi^2$ minimal (Abell 1651 with $\Delta\chi^2 = 38$ and Abell 2721 with $\Delta\chi^2 = 19 - 84$ for data from two different years). Abell 1651 is the cluster from our original pilot study in which we found that the BCG showed no strong evidence of departure from $r^{1/4}$ (Gonzalez et al. 2000). We list in Table 5 the Sérsic parameters derived in both studies of this BCG, noting that the results are consistent despite different modelling procedures and bandpasses.

4.1.2. 2-deV versus Sérsic

Although the Sérsic profile is superior to the $r^{1/4}$ model for our BCG sample and provides a fit that is good in absolute terms ($\chi^2_\nu \simeq 1$), the $\Delta\chi^2$ values in Table 4 argue that the 2-deV profile provides the best parametric fit to the data. With five additional degrees of freedom, the 2-deV profile decreases χ^2 by an average 1039 relative to the Sérsic profile, which is highly significant. The reasons that the 2-deV model provides a superior fit can be assessed by inspection of Figures 3–6. For roughly a third of the galaxies the two components are required to reproduce the observed large gradients in the ellipticity and/or position angle. In the other two-thirds, where these gradients are small, the fit is still statistically superior. The 2-deV model is thus preferred due to both its ability to fit the mean surface brightness profile and improved ability to reproduce the gradients.

4.1.3. Physical interpretation of 2-deV model

Does the success of the 2-deV model imply that there are two physically distinct components? Perhaps the ellipticity gradients and isophotal twists are simply the result of viewing triaxial galaxies off-axis. If so, then the individual components are not physical but rather a convenient means of approximating a triaxial stellar distribution. There are several reasons to conclude that this is not the case. First, there are radial regions over which the position angle and ellipticity are constant (e.g. Abell 2571), which implies that at those radii we are either viewing the system along a principal axis or else that the system is not triaxial (see Figures 5–6). If the former, then the ellipticity and position angle should remain constant at all radii. Second, the more dramatic position angle shifts (e.g. Abell 2571, Abell 3166) happen very suddenly, which again should not be the case for a triaxial system. Third, the apparent position angle of a triaxial body is in general different than the projected position angle of the true major axis. The known correlation between BCG and cluster orientation (Binggeli 1982) argues against these galaxies being strongly triaxial systems viewed at random angles. Fourth, if we are viewing projected triaxial ellipsoids, then we should expect all the galaxies to show position angle swings, as is true with most ellipticals. Many of the BCGs in this sample in fact lack significant position angle gradients, and it is statistically quite improbable that we are viewing such a large fraction along their principal axes. Finally, for a triaxial system the relative importance of the apparent second component should be a strong function of viewing angle (i.e. when the BCG is observed near the principal axis this component should be

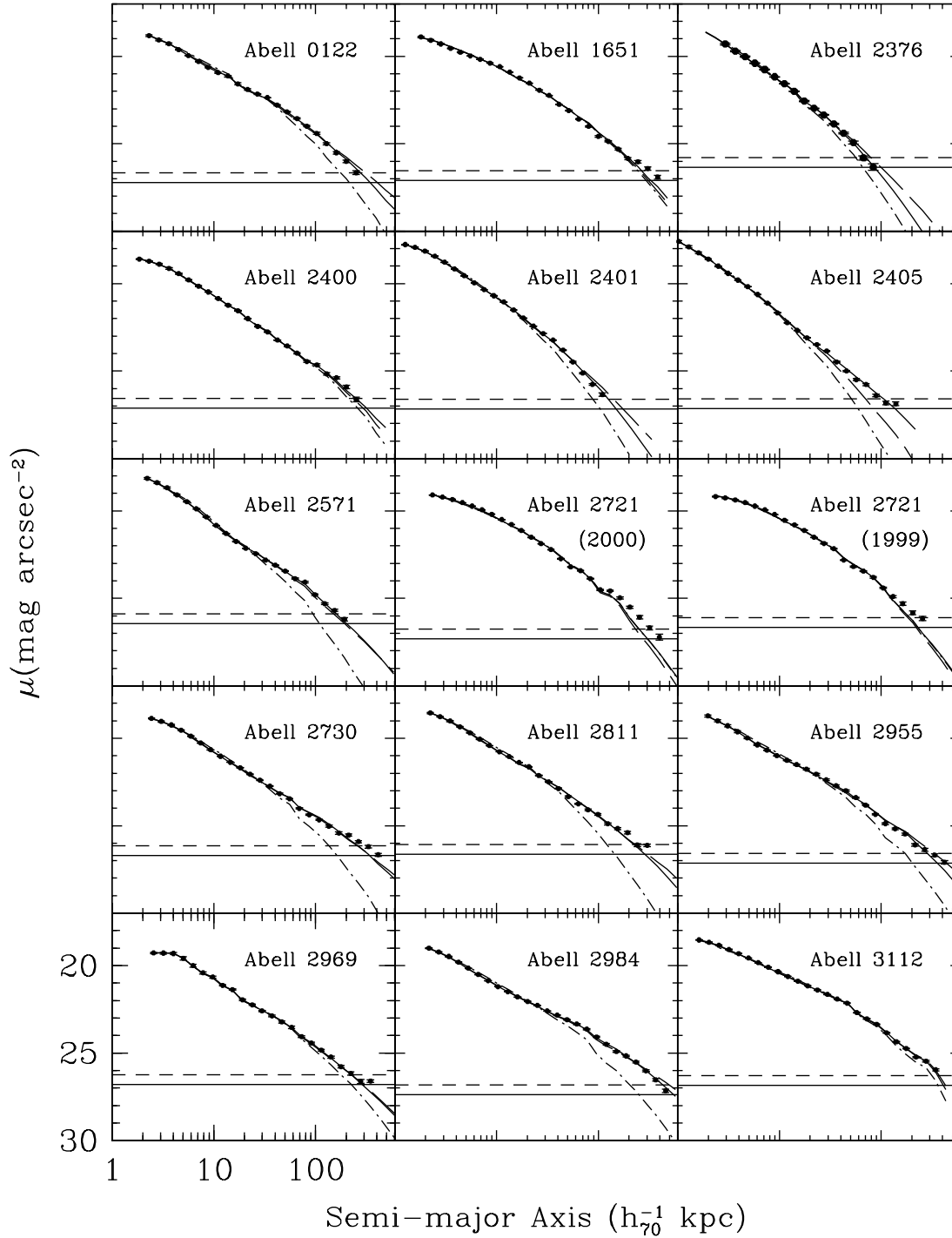


FIG. 3.— I -band surface brightness profiles for the 24 BCGs modelled in this paper. The error bars, which are typically smaller than the symbols, are statistical. Overlaid are the corresponding surface brightness profiles for the best-fit two-dimensional models. We emphasize that these are not fits to the one-dimensional profile, but rather measurements of the two-dimensional models taken in the same apertures as for the data. The $r^{1/4}$ profile (short-long dashed) is a poor representation of the data in most cases, while the $r^{1/n}$ (dotted) and 2-deV (solid) profiles provide improved fits. The solid and dashed horizontal lines correspond to the 3 σ and 5 σ sky level uncertainties, respectively.

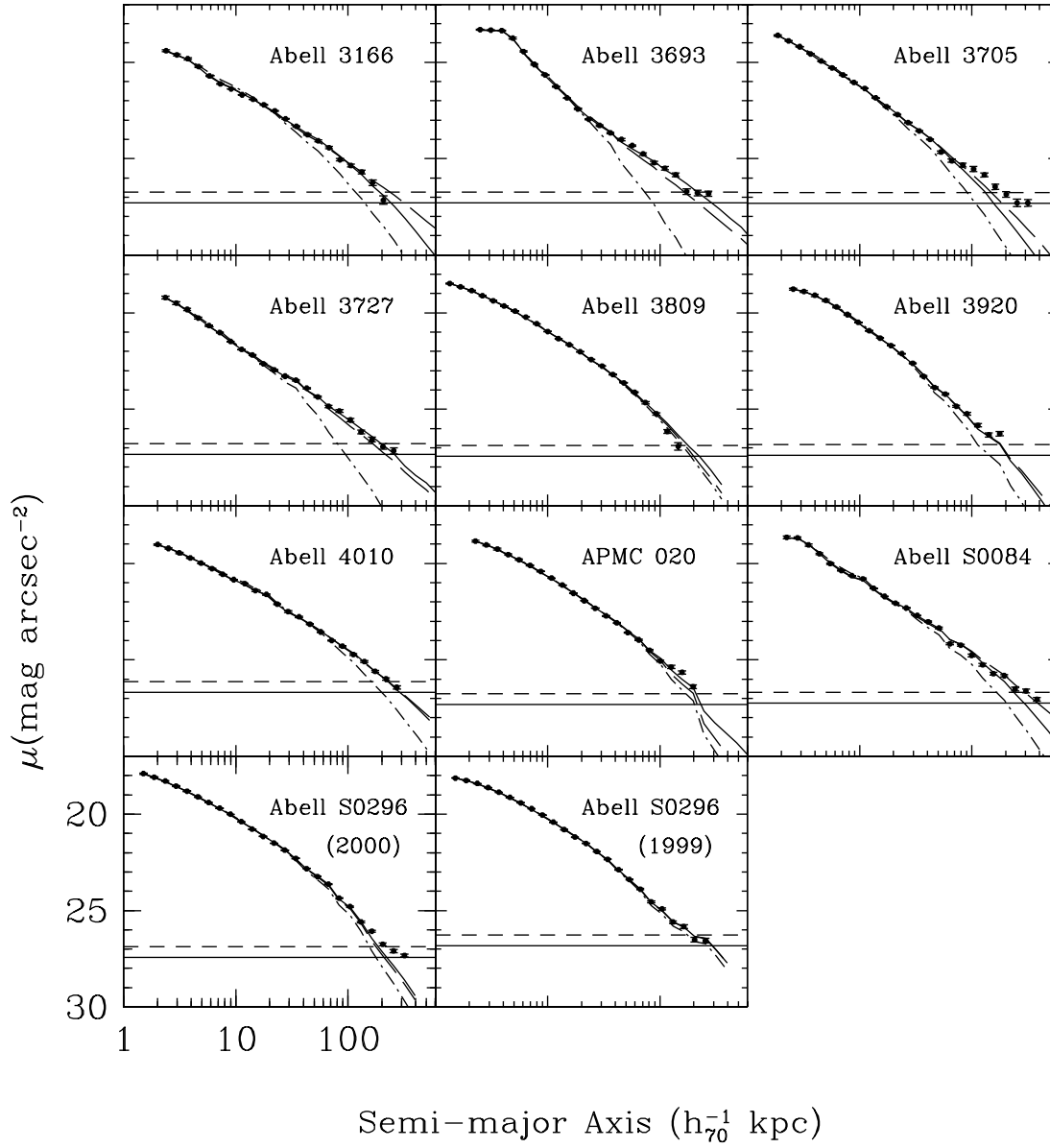


FIG. 3.— Continued.

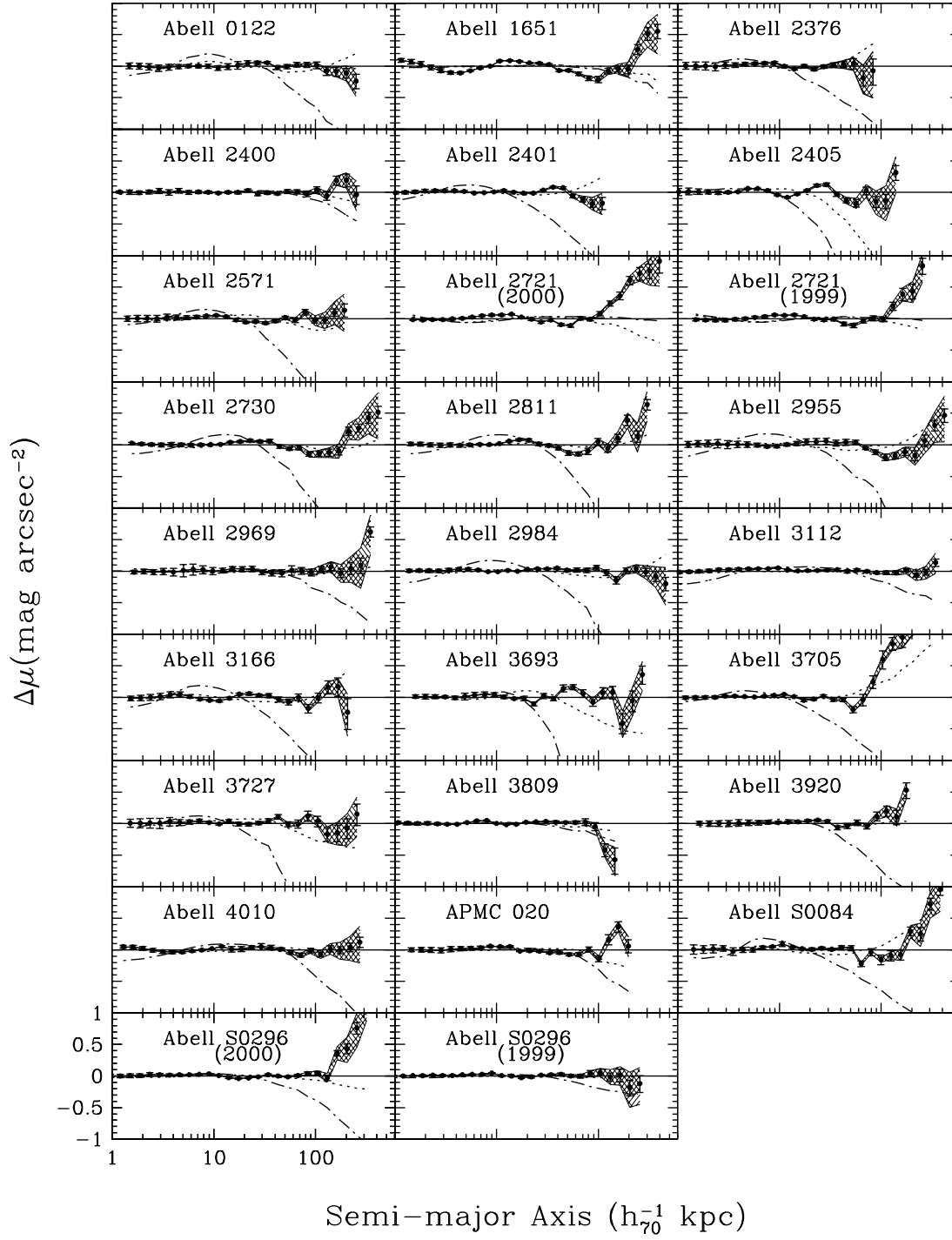


FIG. 4.— Surface brightness residuals relative to the 2-deV model. The line types are the same as in Figure 3, but we have now also added a shaded region denoting the 1σ systematic sky level uncertainty. We note that in two cases, Abell 2721 and Abell 3705, bright saturated stars appear to skew the residuals at large radii. In both cases the stellar PSFs were subtracted and the central regions masked, but the systematic sky level uncertainty is likely larger than our estimate in these cases.

negligible). We find instead that the scale lengths of the two components are strongly correlated (see §4.3).

Aside from the above arguments against the observed gradients in ellipticity and position angle being due to triaxiality,

ancillary data also favor the two components having physical significance. Most compelling are the velocity dispersions in two nearby clusters, Abell 2029 (Dressler 1979) and Abell 2199 (Carter & Bridges 1999; Kelson et al. 2002), which are

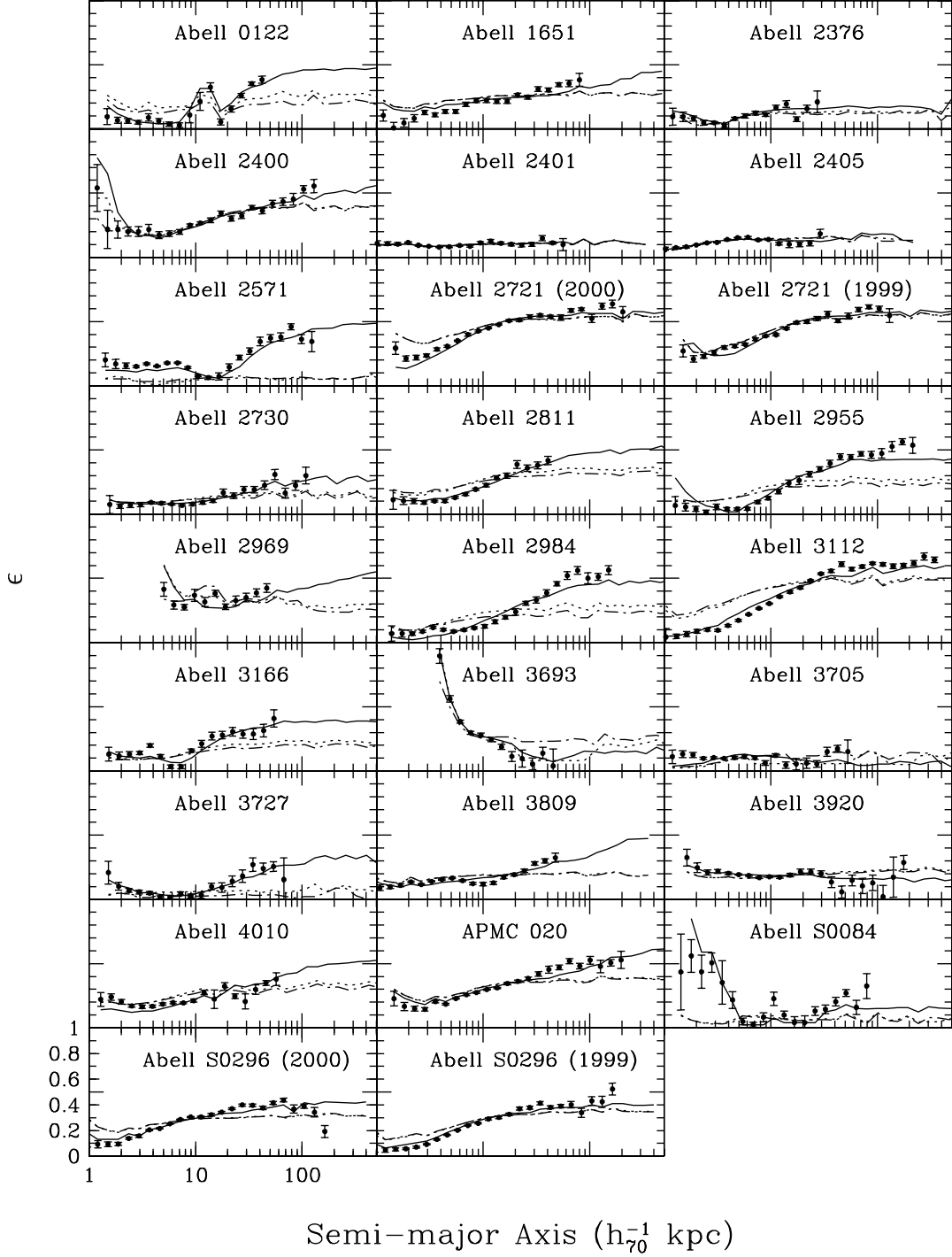


FIG. 5.— Ellipticity profiles for the 24 BCGs modelled in this paper. The line types are the same as in Figure 3. Note that the sharp, non-monotonic changes in ellipticity and position angle seen in a few of the profiles (e.g. Abell 0122) occur when a significant fraction of the data at that radius are masked. These features are thus more a function of the masking than indicative of the profiles, but are produced in both the model and data profiles since the same masking is applied in both cases. In contrast, large monotonic changes in the ellipticity (e.g. Abell 3112) are physical in origin. The 2-deV profile is best able to reproduce these large monotonic changes.

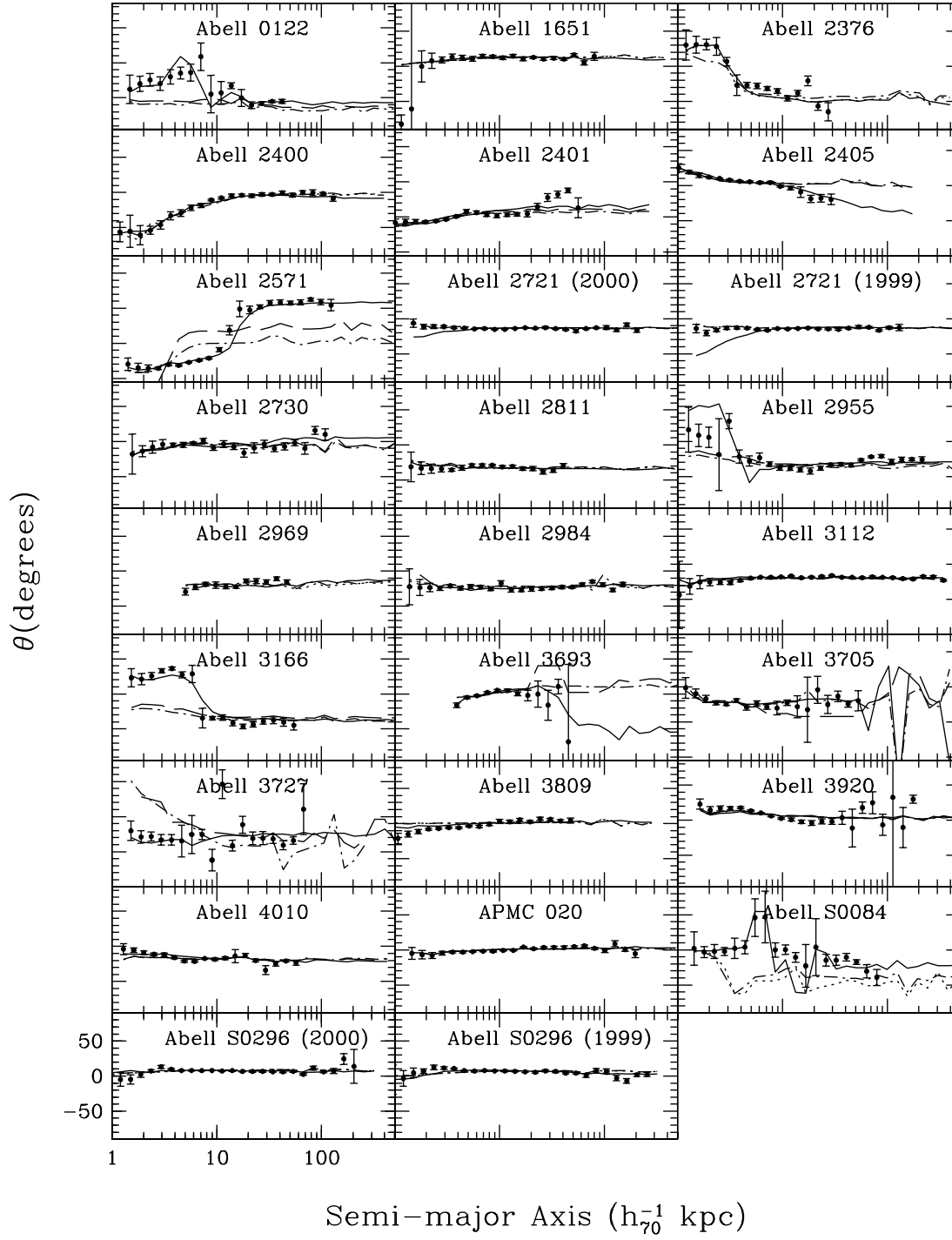


FIG. 6.— Position angle as a function of radius. The line types are the same as in Figure 3. The zeropoint for θ is arbitrary for each galaxy, and is defined to avoid having θ wrap around the vertical axis. Only the 2-deV profile can reproduce the large, rapid position angle changes seen in some of the profiles.

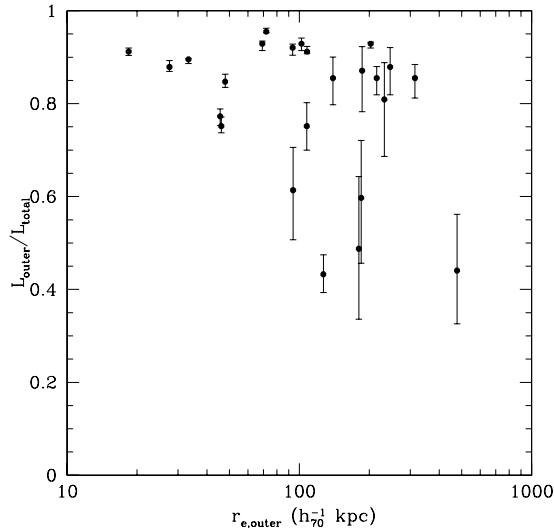


FIG. 7.— Fractional luminosity contribution of the outer component, where L_{total} is defined as the combined luminosity of the inner and outer components. The outer component in most cases contains $>80\%$ of the luminosity.

observed to rise towards the cluster velocity dispersion at large radii. Such a rise is strong evidence that the orbits of the outer stars are associated with the gravitational potential of the cluster rather than the central galaxy. Taken with the arguments against triaxiality, these data argue that the success of the 2-deV model is not simply a result of analyzing triaxial bodies, but rather that these two components are indeed distinct physical entities.

Finally, we emphasize three additional points. First, while we model the two components as a pair of $r^{1/4}$ profiles, we are *not* specifically concluding that the two components are $r^{1/4}$ in nature. This model simply provides an adequate description of our data with a minimum number of free parameters. The outer component could conceivably be better described by an NFW profile (Navarro, Frenk, & White 1996, 1997), but we have not yet explored this model. Second, for any single BCG, we caution the reader to not place undue significance on the structural parameters of the individual components in the 2-deV model. While the results are robust for the statistical sample, the decomposition for a given BCG may be biased by internal surface brightness structures or tidal features. Third, we are not claiming to see the dramatic profile breaks characteristic of classical cD envelopes (e.g. Schombert 1986, 1988) as ubiquitous features. The transition between the two components in our data is typically much more subtle.

4.1.4. Evidence for additional components

Given that we find a two component model to be statistically superior, one can ask whether there is evidence for any additional components. The residuals in Figure 4 indicate that in a few cases the flux exceeds the best-fit model by several sigma in the outermost few radial bins. In two of these cases, Abell 2721 and Abell 3705, the likely origin of this excess is residual flux from saturated stars at the corresponding radii. In another, Abell S0296, only the 2000 observations show an excess, indicating that the origin is likely instrumental rather than physical. The other two cases with $\sim 2\sigma$ excesses (Abell 1651 and Abell S0084) lack a similar explanation, and we also note that the sample as a whole exhibits a slight tendency for

excess flux at large radii. With the current data, however, we cannot discern whether these excesses are due to a systematic error or a true physical excess relative to the model, arising from either an additional component or the outer profile having a form other than $r^{1/4}$.

4.2. Relative Properties of the Two Components

4.2.1. Luminosities

What fraction of the light does the outer component contribute? Figure 7 demonstrates that the outer component typically contains $\sim 80-90\%$ of the total light from both components. In only five cases is the outer component's luminosity $<70\%$ of the total, and those systems tend to be the ones with the largest uncertainties in the magnitude of the outer component (e.g. Abell 1651, Abell 2400, Abell 2405, APMC 020). In subsequent plots we mark these five systems with starred plots to illustrate the impact of this systematic difference in luminosity ratio (whether real or due to an error in decoupling the two components).

4.2.2. Effective Radii

How do the effective radii of the two components compare and are they correlated? The range of effective radii for the inner component is $1-48$ kpc, while the range for the outer component is $18-480$ kpc. Figure 8 shows that the effective radii of the two components are coupled, with a typical ratio $r_{e,outer}/r_{e,inner} \sim 10-40$. For comparison, we overlay a line denoting the ratio of the projected half-mass radii for the dark matter and stellar components ($r_{DM}/r_{stellar} = 13.2$) from the cluster simulation of Dubinski (1998). This simulation recovered a purely $r^{1/4}$ BCG profile, with a scale comparable to that of the inner components observed in this study, but the stellar component was not modelled with sufficient resolution to produce excess light at large radii.

4.2.3. Fundamental Planes

Do the individual components in the 2-deV model independently obey a $\langle \mu \rangle < -r_e$ relation similar to the projection of the elliptical galaxy fundamental plane? We find that both components do indeed form tight $\langle \mu \rangle < -r_e$ relations, as seen in Figure 9a. The slope of the relation for the inner component is consistent with the elliptical fundamental plane, which has $\langle I \rangle > \propto r_e^{-1.22}$ (Jørgensen, Franx, & Kjaergaard 1996). In contrast, the slope of the relation for the outer component is steeper than for elliptical galaxies. If we exclude systems in which the outer component contributes less than two-thirds of the total luminosity (see §4.2.1 above), the slope of the relation is $\langle I \rangle > \propto r_e^{-1.5}$ and the scatter is consistent with the observational uncertainties (Figure 9b).

4.2.4. Ellipticities and Position Angles

Two other parameters of basic interest are the ellipticities and relative offsets in position angle of the two components. The outer component is generally more elliptical than the inner component (Figure 10a), consistent with previous observations that found increasing ellipticity with radius (c.f. Porter, Schneider, & Hoessel 1991). The ellipticity of the outer component is comparable to typical observed ellipticities for the distribution of cluster galaxies (Carter & Metcalfe 1980; Plionis, Barrow, & Frenk 1991; Buote & Canizares 1996; Basilakos, Plionis, & Maddox 2000).

The inner and outer components are closely aligned ($\Delta\theta < 10^\circ$) for roughly 40% of our sample, indicating that both may

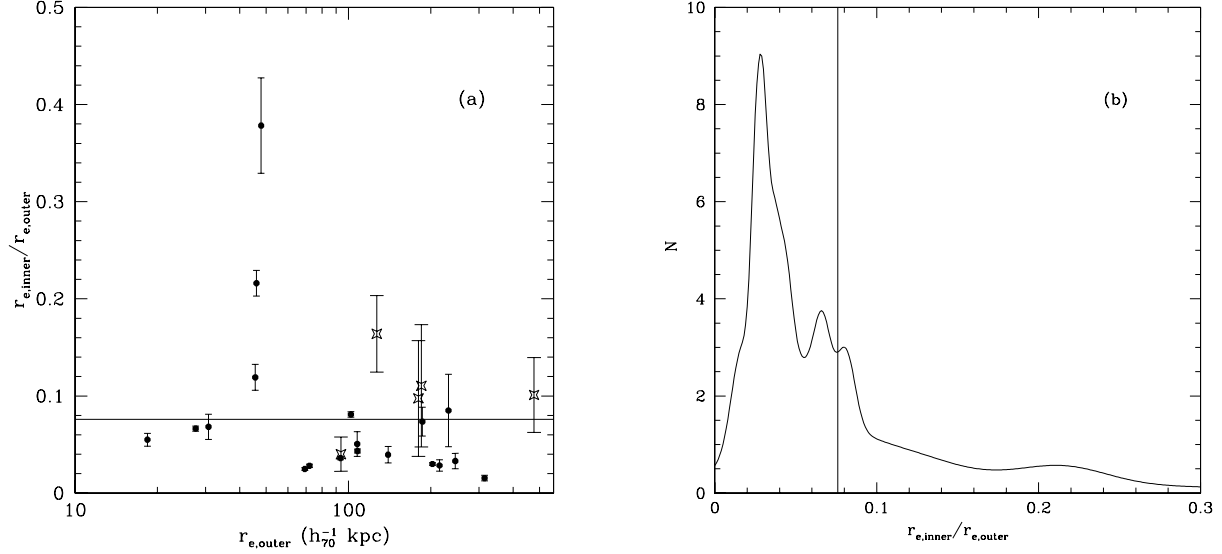


FIG. 8.— (a) Ratio of the effective radii for the inner and outer components. The open starred points correspond to galaxies in which the outer component contains less than two thirds of the total luminosity (see Figure 7), and the solid line corresponds to the ratio between the effective radii of the stellar and dark matter distributions in the BCG simulation of Dubinski (1998). The highest point is the BCG in Abell 2721. For this galaxy both the position angle and axis ratio differences between the two components are small ($|\Delta\theta| < 10^\circ$ and $\Delta b/a < 0.1$), limiting our leverage in separating the two components. (b) Smoothed distribution of $r_{e,inner}/r_{e,outer}$. Each galaxy is represented as a gaussian with $\sigma = 2 \times (\sigma_{statistical}^2 + \sigma_{sky}^2)^{1/2}$. The factor of 2 is an arbitrary scaling factor introduced to yield a smooth distribution. The solid line is the same as in (a). The distribution is strongly peaked at $r_{e,inner}/r_{e,outer} \simeq 35$, suggesting that the two physical scales are correlated.

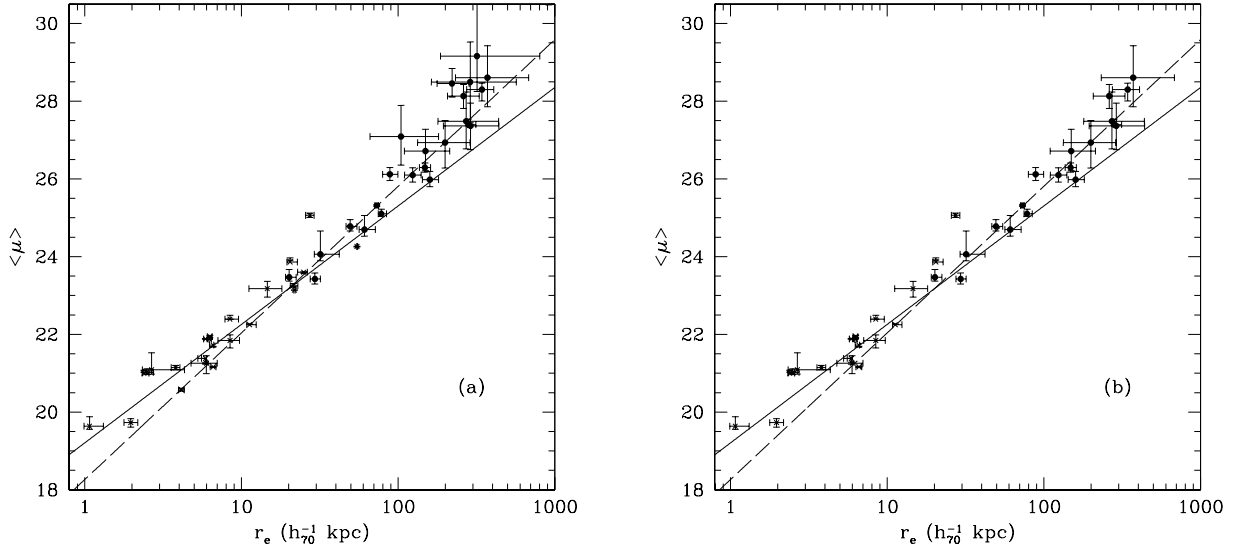


FIG. 9.— Surface brightness vs effective radius for the 2-deV model. Crosses and filled circles denote the inner and outer components, respectively. The lefthand panel (a) shows all galaxies, while the righthand panel (b) shows only those with $>2/3$ of the total luminosity in the outer component. The solid line ($\langle I \rangle \propto r_e^{-1.22}$) corresponds to the relation for ellipticals from Jørgensen, Franx, & Kjaergaard (1996). The dashed line ($\langle I \rangle \propto r_e^{-1.5}$) is a best fit to the outer component data in (b). We note that the inner component data point that lies well above the canonical relation corresponds to Abell 2721, which also has an anomalously large ratio of inner to outer effective radii (see Figure 8). For Abell 2721 both the position angle and axis ratio differences between the two components are small ($|\Delta\theta| < 10^\circ$ and $\Delta b/a < 0.1$), limiting our leverage in separating the two components. We conclude that the inner and outer components both obey tight $\langle \mu \rangle \propto -r_e$ relations. The slope of the relation for the inner component is comparable to the projection of the elliptical fundamental plane, while the slope for the outer component is steeper. Note that in this and all subsequent figures that plot parameter correlations the true parameter uncertainties are correlated and should formally be plotted as correlated error ellipsoids. The error bars that we plot correspond to the 1σ uncertainties in each parameter, derived by adding in quadrature the statistical and systematic sky level uncertainties.

retain information about the initial infall direction of the system (Figure 10b). Those inner components that are not well-aligned show a preference for large $\Delta\theta$ ($\Delta\theta > 45^\circ$ with a distribution that rises toward 90°). This offset may be the result of infall events along other directions that determine the cur-

rent position angle of the central galaxy. It is also possible that this could be a simple projection effect in some cases — particularly cases in which $\Delta\theta \sim 90^\circ$ and $b/a > 0.9$ (e.g. Abell 3727).

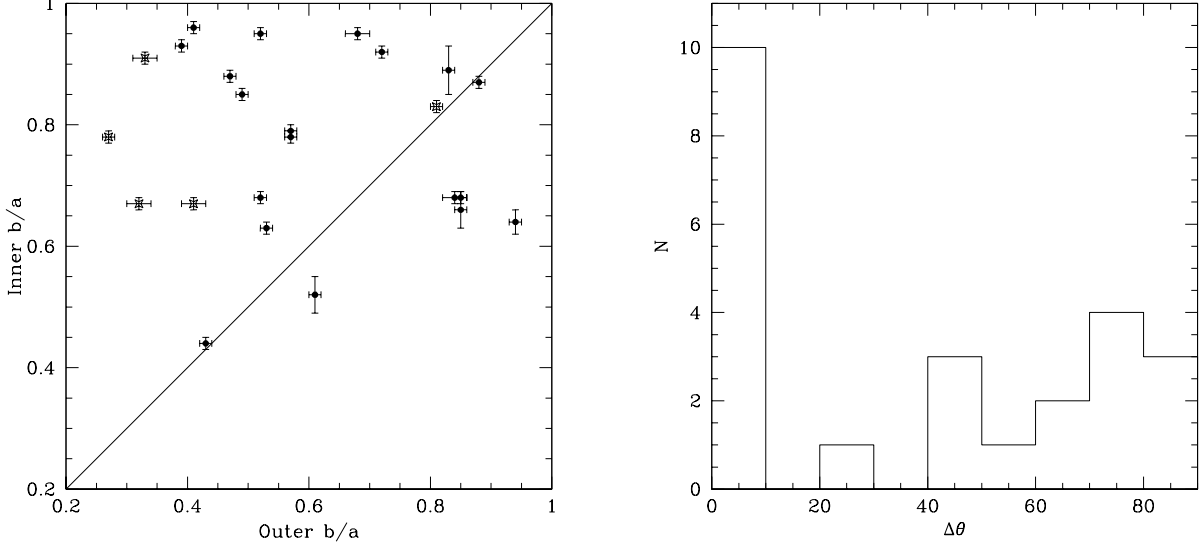


FIG. 10.— (a) Axis ratios of the inner and outer components. The outer component is typically flatter than the core. The symbols are the same as in Figure 8. (b) The distribution of position angle offsets between the inner and outer components. The inner and outer components are aligned to within 10° in approximately 40% of the BCGs.

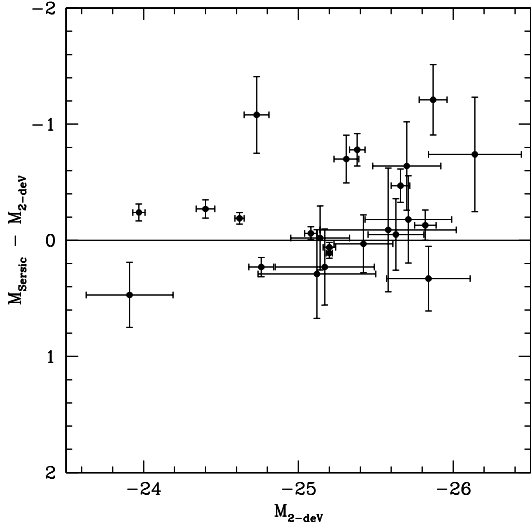


FIG. 11.— Difference in absolute magnitudes between the Sérsic and 2-deV models. The magnitudes are comparable for 75% of the galaxies, while for the other 25% the Sérsic magnitudes are >0.5 mag brighter.

4.2.5. Centroid Offsets

Finally, are the two components concentric? When modelling these galaxies with GALFIT we allowed the centroids of the inner and outer components to vary independently. We find that the two components are concentric to within $1.2''$ (less than the seeing FWHM) in all but one case. The exception is Abell 1651, in which the centroids are offset by $9''$ (~ 15 kpc).

4.3. Biases Arising from One-Component Models

In preceding sections we discerned that the 2-deV model provides a better representation of the typical BCG surface brightness distribution than do $r^{1/4}$ or $r^{1/n}$ profiles, and quantified the properties of the components in this model. We now

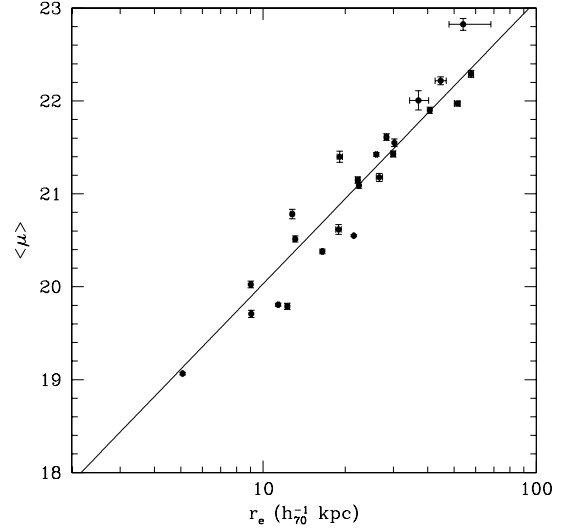


FIG. 12.— Surface brightness vs. effective radius for the single $r^{1/4}$ parameterization. The slope of the solid line corresponds to the $\langle \mu \rangle - r_e$ relation from Jørgensen, Franx, & Kjaergaard (1996), assuming constant velocity dispersion and arbitrarily normalized to match the present data. Despite the failure of the $r^{1/4}$ model at large radii, this parameterization yields a tight $\langle \mu \rangle - r_e$ relation with a slope similar to the relation for normal elliptical galaxies.

return to the single component models, both to facilitate comparison with previous work and to explore the relative biases that arise from using these different models.

4.3.1. Effects on Total Magnitude

How does the choice of parametric model influence the total magnitude derived for the brightest cluster galaxy? The bulk of published BCG photometry assumes either an $r^{1/4}$ or $r^{1/n}$ profile to calculate a total magnitude. The $r^{1/4}$ model obviously underestimates the total luminosity relative to the Sérsic

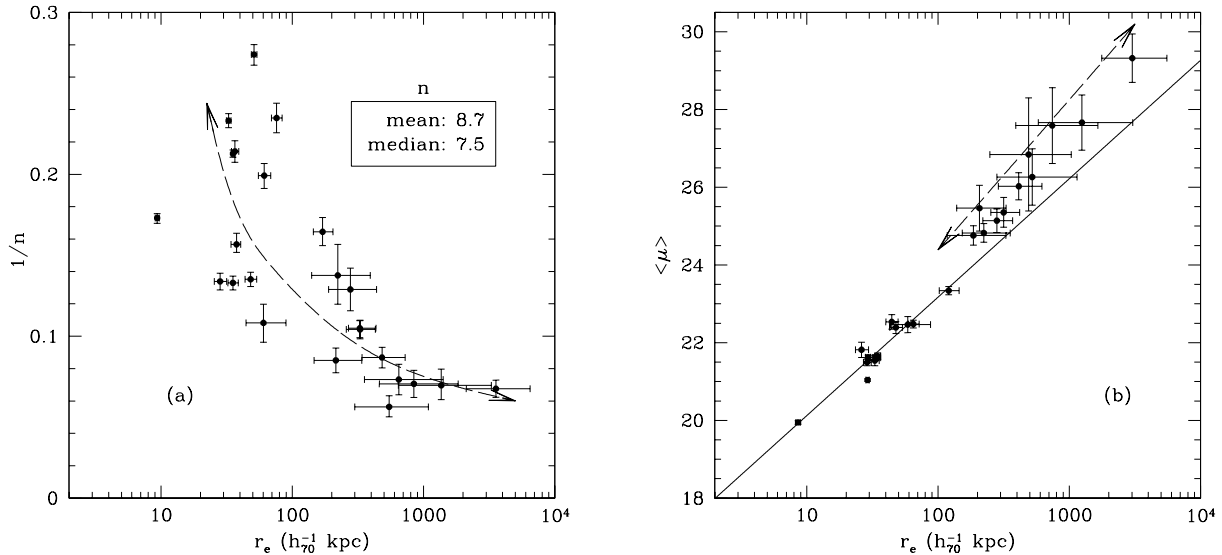


FIG. 13.— Parameters for the Sérsic model. (a) Sérsic index vs. effective radius. The dashed arrow illustrates the intrinsic correlation between r_e and $1/n$ in the Sérsic model. To generate this correlation vector we fit models to a single galaxy multiple times with n fixed to different values. The data indicate that the true uncertainties in the Sérsic parameters are dominated by degeneracies among the correlated parameters and are larger than the quoted uncertainties. Note that the length of the correlation vector is *not* meant to correspond to the size of the correlated uncertainties, but is simply set to span the range of observed r_e values. (b) Surface brightness vs. effective radius. The solid line is the same as in Figure 12, while the dashed arrow again indicates the correlation vector associated with changes in n . For large effective radii the data lie parallel to this correlation vector. It is thus difficult to decouple any true deviation from the FP relation from correlated errors.

and 2-deV models, while Figure 3 argues that in most cases the Sérsic and 2-deV models should yield similar total magnitudes. Figure 11 demonstrates that this expectation is correct for roughly three quarters of the galaxies. For the other 25%, the magnitudes derived from the Sérsic parameterization are more than half a magnitude brighter (albeit typically with large uncertainties). In these cases, the optimal Sérsic models have $n \gtrsim 9$ and thus contain significant luminosity at $r > 300$ kpc (i.e. outside the fitting region).

Table 6 lists the ensemble average and dispersion in the total magnitudes derived using each parameterization. We also include in this table the magnitudes within circular metric apertures of radii 300, 50, and 10 kpc. Within the metric apertures the Sérsic and 2-deV models yield consistent magnitudes and dispersions, while the $r^{1/4}$ model underestimates the flux by $\sim 30\%$ within the 300 kpc aperture. For the total magnitudes, the Sérsic model yields significantly larger scatter, which is a consequence of the extrapolation at $r > 300$ kpc for the galaxies with large n described above. We note that the dispersions for the smallest apertures are consistent with Postman & Lauer (1995), who found a dispersion of 0.327 mag within a metric aperture of $10 h_{100}^{-1}$ kpc.

4.3.2. Effects on the Fundamental Plane

What is the effect of fitting a one-component model on the fundamental plane derived for BCGs? Figure 12 shows the $\langle \mu \rangle - r_e$ relation for the single de Vaucouleurs model, which has a slope similar to that of the $\langle \mu \rangle > -r_e$ projection of the fundamental plane (FP) for normal elliptical galaxies (Jørgensen, Franx, & Kjaergaard 1996). It is interesting to note that the galaxies roughly obey a fundamental plane type relation for the $r^{1/4}$ fit despite the demonstrated inferiority of this model. Figure 13 shows the $1/n - r_e$ and $\langle \mu \rangle - r_e$ relations for the Sérsic model. Because all three parameters are strongly correlated, we explore the impact of changing n on

the other parameters. The additional degree of freedom provided by n yields much larger effective radii (the largest r_e in the $r^{1/4}$ fits is < 60 kpc) and fainter surface brightnesses (the faintest $\langle \mu \rangle$ in the $r^{1/4}$ fits is < 23). The slope of the $\langle \mu \rangle - r_e$ relation is comparable to the direction of the overlaid correlation vector at large r_e (i.e. large n), making any true deviation from the FP relation difficult to decouple from correlated errors arising from uncertainty in n . The scatter in the $1/n - r_e$ plot is also predominantly along the direction of the correlation vector. Together these plots illustrate a key limitation of the Sérsic model for this analysis — namely that systematic variations in n can induce large correlated uncertainties in the other parameters.

5. CONCLUSIONS

Using highly uniform photometric data, we study the surface brightness distribution of the brightest cluster galaxy (BCG) in each of 30 clusters at $0.03 < z < 0.13$ that span a range of velocity dispersions and Bautz-Morgan types. In this first paper, we focus on the 24 clusters for which there is a single, dominant BCG and no evidence of a substantial ongoing merger of subclusters. We employ full two-dimensional fitting to model the surface brightness profiles of these galaxies and their stellar halos within $r = 300$ kpc. From this analysis, we reach several conclusions regarding the nature of the diffuse optical light in clusters:

1. The observed profiles are well described by a *two-component* model consisting of two $r^{1/4}$ profiles with different scale lengths, ellipticities, and orientations. This model yields significantly lower χ^2 than single $r^{1/4}$ or $r^{1/n}$ profiles and reproduces the position angle and ellipticity gradients observed in these galaxies. The nature of these gradients is such that they are unlikely to originate from viewing a single component triaxial system at random (§4.1). We conclude that the two components should be considered physically distinct.

2. The inner component is clearly associated with the BCG. This component is structurally similar to a normal bright elliptical galaxy. The slope of the $\langle \mu \rangle - r_e$ projection of the fundamental plane is consistent with published results over a comparable range of radii ($r_e \approx 1 - 30$ kpc), and the observed axis ratios ($b/a = 0.77 \pm 0.14$) are comparable to those observed in normal ellipticals (Porter, Schneider, & Hoessel 1991).

3. The outer component is consistent with arising from a population of intracluster stars. This intracluster light (ICL) component dominates the luminosity, containing roughly 80-90% of the total light of the two components. The large physical scale of the ICL component ($r_e \approx 20 - 500$ kpc) is similar to that expected for the dark matter distribution (Dubinski 1998) and is thus consistent with the picture in which the intracluster stars trace the global cluster potential. The ICL component exhibits a tight $\langle \mu \rangle - r_e$ relation, but with a steeper slope than the corresponding projection of the elliptical galaxy fundamental plane ($\langle I \rangle \propto r_e^{-1.5}$ compared to $\langle I \rangle \propto r_e^{-1.22}$, respectively). The ICL component is typically more elongated than either the inner BCG component or normal ellipticals, with axis ratios comparable to those observed for the distribution of cluster galaxies (Binggeli 1982). The existence of a distinct ICL component associated with the cluster potential is further bolstered by kinematic data that detect rising velocity dispersions at $r \gtrsim 10$ kpc in several systems (Abell 2029, Dressler (1979); Abell 2199, Carter & Bridges (1999); Kelson et al. (2002)), presumably due to the transition from the bound stellar population of the BCG to the intracluster stellar population.

4. The inner and outer components are strongly aligned ($|\Delta\theta| < 10^\circ$) in roughly 40% of the clusters. When they are not aligned, the components tend toward high degrees of misalignment, suggesting that accretion of infalling material may change the orientation of some BCGs for a time.

5. The ratio of scale-lengths for the outer and inner components, $r_{e,outer}/r_{e,inner}$, is $\approx 10 - 40$, with the distribution strongly peaked at $r_{e,outer}/r_{e,inner} = 35$.

Recent hydrodynamic simulations incorporate much of the relevant physics necessary to produce populations of intracluster stars, and thus provide quantitative predictions for the properties of the ICL. These simulations agree on several interesting points. Consistent with previous theoretical work (c.f. Richstone & Malamuth 1983; Miller 1983), the simulations predict that intracluster stars produce roughly 20-50% of the total cluster luminosity and originate from tidal stripping (Sommer-Larsen, Romeo, & Portinari 2004; Murante et al. 2004; Willman et al. 2004). The intracluster stars in these simulations form at higher median redshift than stars that remain in cluster galaxies at $z = 0$, concentrate more toward the cluster center than the galaxies, and exceed the stellar mass density within about half the virial radius (Sommer-Larsen, Romeo, & Portinari 2004; Murante et al. 2004). Additionally, formation of the ICL component is found to be a continuing process, with significant

growth in luminosity since $z=1$ (Willman et al. 2004).

We confirm that the ICL is a ubiquitous feature for clusters with a single, dominant BCG, demonstrate that it dominates the combined luminosity of the BCG+ICL components, and quantify some of the properties of the ICL. Recent work by Feldmeier et al. (2004) indicates that intracluster light is also prevalent in clusters without dominant central galaxies, and thus together these studies confirm that ICL is a generic feature of the cluster environment. Our measurements of the extent of the ICL component and its elongation, which is similar to published cluster galaxy spatial distributions, further indicate that the evolution of the ICL is tied to the cluster as a whole rather than to the BCG.

Finally, we emphasize that understanding the growth and accretion of brightest cluster galaxies and the intracluster stellar populations is also of direct relevance to studies of lower mass elliptical galaxies. Graham et al. (1996) interpreted the large Sérsic indices observed at $r \lesssim 25$ kpc for their BCG sample as the extension of an empirical correlation between n and galaxy mass observed by Caon, Capaccioli, & D’Onofrio (1993) for other elliptical galaxies, and Graham, Erwin, Caon, & Trujillo (2001) have presented evidence for a correlation between n and the central black hole mass. We have now demonstrated that similarly large Sérsic indices are obtained when BCGs are modelled to much larger radii. Because the outer component in the 2-deV model contributes a significant fraction ($>35\%$) of the total luminosity within $r = 25$ kpc for 75% of the BCGs in our sample, we argue that these large Sérsic indices are better interpreted as arising from the dominance of this intracluster component at large radii. It is intriguing to consider whether the correlations observed for lower mass systems are partly due to a correlation between galaxy mass and the fractional luminosity existing in halos comprised of stars tidally stripped from lower mass satellites. We suspect that investigation along these lines may provide a physical motivation for the observed empirical correlations.

6. ACKNOWLEDGEMENTS

We are especially grateful for insightful conversations with Alistair Graham and Tod Lauer. We also thank Stefano Zibetti, Simon White, Heinz Andernach, and the anonymous referee for helpful discussions and comments that improved the paper. AHG is supported by an NSF Astronomy and Astrophysics Postdoctoral Fellowship under award AST-0407085. AIZ is supported by NSF grant AST-0206084 and NASA LTSA grant NAG5-11108. DZ acknowledges fellowships from the David and Lucile Packard Foundation and the Alfred P. Sloan Foundation. This publication makes use of data products from the Two Micron All Sky Survey, which is a joint project of the University of Massachusetts and the Infrared Processing and Analysis Center/California Institute of Technology, funded by the National Aeronautics and Space Administration and the National Science Foundation.

REFERENCES

- Basilakos, S., Plionis, M., & Maddox, S. J. 2000, MNRAS, 316, 779A
 Bautz, L. P. & Morgan, W. W. 1970, ApJ, 162, L149
 Bertin, E. & Arnouts, S. 1996, A&AS, 117, 393
 Binggeli, B. 1982, A&A, 107, 338
 Buote, D. A. & Canizares, C. R., 1996, ApJ, 457, 565
 Caon, N., Capaccioli, M., & D’Onofrio, M. 1993, MNRAS, 265, 1013
 Carter, D. & Metcalfe, N. 1980, MNRAS, 191, 325
 Carter, D., Bridges, T. J., & Hou, G. K. T. 1999, MNRAS, 307, 131
 Dressler, A. 1979, ApJ, 231, 659
 Dubinski, J. 1998, ApJ, 502, 141
 Feldmeier, J. J., Mihos, J. C., Morrison, H. L., Rodney, S. A., & Harding, P. 2002, ApJ, 575, 779
 Feldmeier, J. J., Mihos, C., Morrison, H. L., Harding, P., Kaib, N., & Dubinski, J. 2004, astro-ph/0403414
 Gallagher, J. S. & Ostriker, J. P. 1972, AJ, 77, 288
 Gonzalez, A. H., Zabludoff, A. I., Zaritsky, D., & Dalcanton, J. J. 2000, ApJ, 536, 561
 Graham, A., Lauer, T. R., Colless, M., & Postman, M. 1996, ApJ, 465, 534

- Graham, A. W., Erwin, P., Caon, N., & Trujillo, I. 2001, *ApJ*, 563, L11
 Jørgensen, I., Franx, M., & Kjaergaard, P. 1996, *MNRAS*, 280, 167
 Kelson, D. D., Zabludoff, A. I., Williams, K. A., Trager, S. C., Mulchaey, J. S., & Bolte, M. 2002, *ApJ*, 576, 720
 Mathews, Morgan, & Schmidt 1964
 Malamuth, E. M., Richstone, D. O. 1984, *ApJ*, 276, 413
 Merritt, D. 1984, *ApJ*, 276, 26
 Miller, G. E., 1983, *ApJ*, 268, 495
 Murante et al. 2004, *astro-ph/0404025*
 Navarro, J. F., Frenk, C. S., & White, S. D. M. 1997, *ApJ*, 462, 563
 Navarro, J. F., Frenk, C. S., & White, S. D. M. 1997, *ApJ*, 490, 493
 Oemler, A. Jr. 1973, *ApJ*, 180, 11
 Oemler, A. Jr. 1976, *ApJ*, 209, 693
 Plionis, M., Barrow, J. D., & Frenk, C. S. 1991, *MNRAS*, 249, 662
 Porter, A. C., Schneider, D. P., & Hoessel, J. G. 1881, *AJ*, 101, 1561
 Postman, M. & Lauer, T. 1995, *ApJ*, 440, 28
 Richstone, D. O., & Malamuth, E. M. 1983, *ApJ*, 268, 30
 Scheick, X. & Kuhn, J. R. 1994, *ApJ*, 423, 566
 Schombert, J. M. 1986, *ApJS*, 60, 603
 Schombert, J. M. 1987, *ApJS*, 64, 643
 Schombert, J. M. 1988, *ApJ*, 328, 475
 Sommer-Larsen, J., Romeo, A. D., & Portinari, L. 2004, *astro-ph/0403282*
 Starck, J. & Murtagh, F. 1994, *A&A*, 288, 342
 Stetson, P. B. 1987, *PASP*, 99, 191
 Uson, J. M., Bough, S. P., & Kuhn, J. R. 1990, *Science*, 250, 539
 Uson, J. M., Bough, S. P., & Kuhn, J. R. 1991, *ApJ*, 369, 46
 Vikhlinin, A., McNamara, B. R., Forman, W., Jones, C., Quintana, H., & Hornstrup, A. 1998, *ApJ*, 502, 558
 Willman, B., Governato, F., Wadsley, J., Quinn, T. 2004, submitted to *MNRAS*
 Zaritsky, D., Schectman, S. A., & Bredthauer, G. 1996, *PASP*, 108, 104

APPENDIX

ROBUSTNESS OF RESULTS

We now explore whether either our ability to discriminate between models or the resulting model parameters are compromised by systematic errors and compare results for two clusters observed in multiple runs.

Error in the sky level

While GALFIT returns statistical uncertainties, we are undoubtedly limited by *systematic* errors in deriving structural parameters. The most significant source of such errors is the determined mean sky levels. In this section we ask two questions: 1) does systematic error in the sky level degrade our ability to discriminate between Sérsic and 2-deV models, and 2) what is the magnitude of the induced uncertainties in the structural parameters?

We estimated the 1σ uncertainty in the background sky levels in §3.4. To assess whether this degree of uncertainty compromises our ability to discriminate between models, we rerun GALFIT for all models with the sky level artificially altered by $\pm 1\sigma$. We find that the resulting χ^2 differences between the $r^{1/n}$ and 2-deV models are $\Delta\chi^2 = 1039$ and $\Delta\chi^2 = 1089$ when we increase and decrease the sky, respectively, which are consistent with our result from §4 ($\Delta\chi^2 = 1039$). We conclude that the statistical preference for 2-deV models is not a result of systematic error in the sky level.

From the same artificially altered data, we rederive the structural parameters. The errors quoted in parentheses in Tables 2-4 correspond to the variations arising from this change. For the Sérsic model the most sensitive parameters are r_e and n , because a change in the outer structure can mimic a change in the sky level. The derived effective radii and surface brightnesses are relatively robust for cases with $n < 10$, but are highly uncertain for larger indices (see §4.3.2). For the 2-deV model the parameters are remarkably robust. The largest uncertainties arise for the outer component (for the same reason as with the Sérsic model), and the uncertainty is proportional to the effective radius of the outer component. Still, even for the cases where $r_e \gtrsim 300$ kpc (i.e. the size of the fitting region) the uncertainty in r_e is $\lesssim 10\%$. These cases should obviously be viewed with caution (as is always true when the fitting region is $< r_e$), but this robustness is encouraging.

Sensitivity to input PSF

Another concern is whether the results are sensitive to the accuracy of the input PSF. We assess this sensitivity by reanalyzing one of the BCGs (Abell 0122) using PSFs taken from other fields with seeing comparable to within $0.1''$ (Abell 2376, Abell 3727, and Abell S1096). Although drawn from similar seeing conditions, these PSFs are structurally distinct. The optimal 2-deV parameters are listed in Table 7 for each input PSF. The most sensitive parameter is r_e for the inner component, which increases up to 25% when an incorrect PSF is used. We consider 25% to be an approximate upper bound on the systematic uncertainty in the inner r_e due to error in the input PSF. The outer component r_e , and $\langle \mu \rangle$ for both components, agree to within 7% in all cases. Finally, χ^2 changes by $\lesssim 100$, which is significantly less than the differences between the three functional forms tested in this paper.

A different concern is that the PSF convolved with the GALFIT models only extends to $r = 15''$. Could the inclusion of the PSF wings (Figure 1) affect the results? Convolution of the BCG profile with the full PSF including the extended wings increases the surface brightness by $\sim 1\%$ at $r \gtrsim 10''$, which should be small enough to not significantly alter the derived structural parameters. To verify this assumption, we performed modelling tests employing a large PSF that includes these wings. We find that the most sensitive model parameter is the r_e of the outer component in the 2-deV model, which typically decreases by 5–10% when the extended PSF is used. The relative luminosities of the two components also change slightly, with the outer component contributing $\sim 2\%$ less of the total luminosity. In both cases this bias due to using the smaller PSF corresponds to $\lesssim 1\sigma$ changes and thus will not qualitatively alter any of the results described below.

Sensitivity to masking

Might the “second component” observed at large radii be due to residual emission from individual cluster galaxies? If the masking is insufficient, then flux from the outer regions of individual galaxies will appear as a secondary halo in the surface brightness modelling. This component would have an ellipticity and orientation similar to the galaxy distribution, potentially yielding gradients in both quantities as observed in our data.

We test this possibility by varying the degree of masking and measuring the difference in the observed profiles. We perform this test on the BCG in Abell 2571, a galaxy for which the data indicates a significant excess relative to $r^{1/4}$ at $r \gtrsim 20$

kpc. We extend the object masks and increase the fraction of masked pixels from 26% to 53%. The best-fit parameters change by less than the systematic uncertainties derived for changes in the sky level, and the 2-deV model maintains a significantly lower χ^2 than the other models ($\chi_{dev}^2 - \chi_{2-deV}^2 = 4300$ and $\chi_{Sersic}^2 - \chi_{2-deV}^2 = 1745$). The profiles derived using the normal and enhanced masking are also consistent to within the 1σ statistical uncertainties for all radial bins. We conclude that the observed outer component is *not* an artifact arising from insufficient masking of cluster galaxies.

Clusters observed during multiple runs

The two clusters in our sample that were observed in both 1999 and 2000, Abell 2721 and Abell S0296, provide an independent check on the impact of systematics. We model the BCGs independently for each data set and compare the profiles and derived parameters for the BCGs. For both galaxies the azimuthally averaged surface brightness profiles are consistent to within the statistical uncertainties at all radii larger than the seeing. With only two exceptions, the parameters derived from the two data sets are consistent to within the systematic uncertainties for all models (Table 2—4). The only exceptions are the ellipticities for the Sérsic and 2-deV models and the position angle shift, $\Delta\theta$, in the 2-deV model, which differ in some cases by as much $\sim 5\sigma$. We thus caution that the precision (typically ~ 0.01 in ellipticity and \sim few degrees in position angle) may be somewhat overestimated.

The most striking difference is in the $\Delta\chi^2$ values for Abell S0296, which are significantly smaller for the 1999 data set. The likely origin of this discrepancy is the poor data quality for the 1999 observations of this cluster, which, as noted in Table 1, are compromised by large-scale sky variations. Consequently, the comparison for this cluster can be viewed as a worst-case test. Nonetheless, both data sets yield the same qualitative conclusions and comparable structural parameters, which again argues that our results are robust against systematic errors.

TABLE 1
CLUSTER SAMPLE

Cluster	z_{BCG}	BM type	Date of Run	Exposure time (s)	Airmass	FWHM('')	2MASS ID	Comments
Abell 0122	.1127	I	10/2000	635	1.03	1.38	2MASX J00572288-2616528	
Abell 0447	.1123	I	10/2000	667	1.10	1.67		a b
Abell 1651	.0853	I-II	3/1995	285	1.12	1.47	2MASX J12592251-0411460	
Abell 2376	.0891	I-II	10/2000	673	1.19	1.33	2MASX J21460478-0927054	
Abell 2400	.0880	II	10/2000	484	1.05	1.79	2MASX J21574250-1124402	
Abell 2401	.0578	II	10/2000	909	1.07	2.20	2MASX J21582246-2006145	
Abell 2405	.0366		10/2000	698	1.13	1.34	2MASX J21594215-1748019	cd
Abell 2571	.1081	II	11/1999	570	1.15	1.46	2MASX J23183367-0216356	
Abell 2721	.1149	II	11/1999	694	1.01	1.79	2MASX J00055975-3443171	
			10/2000	808	1.03	1.33		
Abell 2730	.120	II	11-12/1999	818	1.08	2.38	2MASX J00095644-3541015	e
Abell 2804	.1121	I-II	12/1999	758	1.11	1.98		b
			10/2000	758	1.03	1.48		
Abell 2811	.1082	I-II	12/1999	432	1.30	2.10	2MASX J00420892-2832087	
Abell 2955	.0945	II	10/2000	695	1.14	1.41	2MASX J01570191-1701234	
Abell 2969	.1271	I	12/1999	756	1.03	2.13	2MASX J02033533-4106002	
Abell 2984	.1044	I	10/2000	870	1.06	1.57	2MASX J02112484-4017261	
Abell 3094	.0683	I-II	10/2000	745	1.02	1.60		b
Abell 3112	.0759	I	12/1999	530	1.23	1.87	2MASX J03175766-4414175	
Abell 3166	.1171	I	10/2000	678	1.04	1.68	2MASX J03464387-3248454	
Abell 3194	.0927	III	10/2000	878	1.03	1.80		b
Abell 3693	.1237		10/2000	806	1.09	1.50	2MASX J20341991-3429387	d
Abell 3705	.0883	III	10/2000	813	1.07	1.41	2MASX J20420438-3513067	
Abell 3727	.1159	III	10/2000	826	1.04	1.37	2MASX J20593652-3629085	
Abell 3809	.0616	III	10/2000	790	1.14	1.37	2MASX J21465904-4353564	
Abell 3920	.1263	I-II	10/2000	878	1.23	2.30	2MASX J22492865-4053335	
Abell 4010	.0963	I-II	11/1999	709	1.03	1.73	2MASX J23311412-3630405	
APMC 020	.1105		10/2000	808	1.05	1.42	2MASX J00133506-3443086	d
Abell S0084	.1087	I	10/2000	763	1.07	1.25	2MASX J00492282-2931069	
Abell S0296	.0699	I	12/1999	514	1.33	2.30	2MASX J02463700-4222015	f
			10/2000	899	1.04	1.44		
Abell S0952	.0898	II	10/2000	813	1.16	1.41		b
Abell S1096	.1049	I-II	10/2000	760	1.15	1.49		b

^aThe BCG in this cluster has a complicated core with multiple nuclei, which are also visible in a *Chandra* image of the cluster.

^bThis BCG is not included in the statistical sample analyzed in this paper.

^cAbell 2405 is a superposition of two relatively poor systems at 11,000 and 27,000 km s⁻¹. Here we focus upon the lower redshift group.

^dNo published Bautz-Morgan type. Abell 2405 and Abell 3693 each have two discrete redshift peaks. Published Bautz-Morgan types do exist for these clusters, but not for the redshift peaks that we are studying.

^eThe listed value is the mean cluster redshift rather than the BCG redshift.

^fThe 1999 data for Abell S0296 are poor. The images contain a large gradient not present in any of the other data.

TABLE 2
DE VAUCOULEURS PARAMETERS

Cluster	M	σ_M	r_e	σ_{r_e}	b/a	$\sigma_{b/a}$	χ^2_ν
Abell 0122	-24.98	0.01 (0.02)	29.9	0.2 (0.5)	0.79	0.01	1.123
Abell 1651	-25.44	0.01 (0.02)	57.7	0.4 (1.1)	0.73	0.01	0.985
Abell 2376	-23.69	0.01 (0.00)	9.0	0.1 (0.1)	0.88	0.01	0.987
Abell 2400	-24.77	0.01 (0.03)	37.0	0.8 (2.9)	0.60	0.01	0.997
Abell 2401	-24.28	0.01 (0.00)	11.4	0.1 (0.1)	0.88	0.01	1.043
Abell 2405	-23.18	0.01 (0.00)	5.1	0.1 (0.0)	0.85	0.01	1.002
Abell 2571	-24.66	0.01 (0.01)	12.3	0.1 (0.2)	0.94	0.01	1.046
Abell 2721 (2000)	-25.19	0.01 (0.01)	40.7	0.3 (0.4)	0.46	0.01	1.020
Abell 2721 (1999)	-25.18	0.01 (0.03)	39.1	0.3 (0.8)	0.45	0.01	1.005
Abell 2730	-25.01	0.01 (0.02)	26.6	0.2 (0.7)	0.86	0.01	1.066
Abell 2811	-24.78	0.01 (0.02)	18.9	0.2 (0.4)	0.68	0.01	1.022
Abell 2955	-24.54	0.01 (0.01)	22.2	0.2 (0.4)	0.77	0.01	1.068
Abell 2969	-24.92	0.01 (0.11)	54.0	0.7 (10.1)	0.71	0.01	1.022
Abell 2984	-24.65	0.01 (0.01)	28.3	0.2 (0.4)	0.77	0.01	1.109
Abell 3112	-25.47	0.01 (0.03)	51.5	0.3 (1.2)	0.52	0.01	0.987
Abell 3166	-24.05	0.01 (0.02)	19.1	0.2 (0.4)	0.80	0.01	1.014
Abell 3693	-24.15	0.01 (0.00)	9.1	0.1 (0.0)	0.75	0.01	1.033
Abell 3705	-24.01	0.01 (0.00)	13.1	0.1 (0.0)	0.86	0.01	1.041
Abell 3727	-23.79	0.01 (0.00)	12.8	0.1 (0.1)	0.97	0.01	1.036
Abell 3809	-24.47	0.01 (0.00)	26.0	0.1 (0.2)	0.80	0.01	1.006
Abell 3920	-24.79	0.01 (0.00)	16.5	0.1 (0.0)	0.78	0.01	0.994
Abell 4010	-25.00	0.01 (0.04)	44.6	0.4 (2.1)	0.68	0.01	1.019
APMC 020	-24.69	0.01 (0.00)	22.4	0.1 (0.2)	0.62	0.01	1.009
Abell S0084	-24.87	0.01 (0.00)	30.2	0.2 (0.0)	0.93	0.01	1.032
Abell S0296 (2000)	-24.97	0.01 (0.00)	21.5	0.1 (0.1)	0.69	0.01	1.053
Abell S0296 (1999)	-24.94	0.01 (0.01)	21.6	0.1 (0.3)	0.65	0.01	0.972

NOTE. — The listed effective radius is $r_e \equiv \sqrt{ab}$ and is in units kpc. The absolute magnitudes, which are total magnitudes that include extrapolation beyond $r = 300$ kpc, are *not* corrected for extinction or k-dimming. Both corrections are typically < 0.1 mag for galaxies in our sample. The column b/a gives the ratio of the minor to major axes. In the last column χ^2_ν is the reduced χ^2 . For clusters observed during multiple years, the ensemble χ^2_ν value includes only the 2000 data. Parameter uncertainties corresponding to the 1σ sky level uncertainties are given in parentheses.

TABLE 3
SERSIC PARAMETERS

Cluster	M	σ_M	r_e	σ_{r_e}	n	σ_n	b/a	$\sigma_{b/a}$	$\Delta\chi_d^2$
Abell 0122	-26.13	0.03 (0.13)	280.7	16.9 (+86.7/-59.9)	9.60	0.14 (+0.57/-0.50)	0.73	0.01	-6032
Abell 1651	-25.51	0.01 (0.07)	65.0	1.3 (+6.7/-5.6)	4.26	0.04 (+0.17/-0.16)	0.73	0.01	-38
Abell 2376	-24.21	0.02 (0.06)	26.2	1.0 (+3.2/-2.8)	7.47	0.11 (+0.31/-0.27)	0.86	0.01	-2073
Abell 2400	-24.94	0.02 (0.07)	47.8	1.4 (+5.7/-4.6)	5.02	0.06 (+0.21/-0.18)	0.61	0.01	-195
Abell 2401	-24.81	0.01 (0.04)	33.3	0.5 (+3.3/-2.7)	7.52	0.04 (+0.26/-0.23)	0.89	0.01	-14411
Abell 2405	-23.44	0.01 (0.02)	8.6	0.1 (+0.3/-0.3)	5.78	0.03 (+0.11/-0.09)	0.84	0.01	-5774
Abell 2571	-25.39	0.02 (0.16)	58.8	2.4 (+28.6/-15.6)	9.24	0.13 (+1.14/-0.89)	0.95	0.01	-4580
Abell 2721 (2000)	-25.09	0.01 (0.04)	34.7	0.6 (+1.8/-1.6)	3.65	0.03 (+0.09/-0.08)	0.46	0.01	-84
Abell 2721 (1999)	-25.12	0.01 (0.07)	35.5	0.7 (+3.3/-3.3)	3.77	0.04 (+0.22/-0.18)	0.45	0.01	-19
Abell 2730	-26.88	0.06 (0.39)	1250.0	177.4 (+1759.3/-661.3)	14.36	0.37 (+2.09/-1.81)	0.84	0.01	-5253
Abell 2811	-26.34	0.06 (0.31)	522.0	75.4 (+607.3/-155.3)	13.65	0.41 (+2.01/-1.55)	0.65	0.01	-3351
Abell 2955	-26.01	0.03 (0.19)	412.5	28.8 (+202.1/-122.2)	11.52	0.17 (+0.91/-0.79)	0.73	0.01	-9107
Abell 2969	-25.67	0.03 (0.30)	185.9	9.3 (+142.8/-68.1)	7.27	0.12 (+1.08/-0.89)	0.70	0.01	-390
Abell 2984	-27.08	0.06 (0.29)	3019.2	374.7 (+2451.5/-223.7)	14.81	0.28 (+1.25/-0.99)	0.72	0.01	-10569
Abell 3112	-25.95	0.01 (0.11)	120.5	2.5 (+24.0/-18.2)	6.08	0.04 (+0.33/-0.31)	0.50	0.01	-3406
Abell 3166	-25.81	0.08 (0.32)	741.5	143.8 (+871.5/-337.0)	14.16	0.52 (+1.93/-1.50)	0.77	0.01	-2693
Abell 3693	-25.68	0.10 (0.25)	489.7	142.3 (+483.2/-223.7)	17.74	1.03 (+2.15/-1.92)	0.80	0.01	-2535
Abell 3705	-24.64	0.02 (0.05)	44.4	1.7 (+4.9/-4.1)	7.40	0.10 (+0.25/-0.23)	0.85	0.01	-3419
Abell 3727	-25.16	0.05 (0.20)	207.1	24.4 (+117.8/-65.8)	11.75	0.32 (+1.15/-0.96)	0.93	0.01	-2494
Abell 3809	-24.53	0.01 (0.02)	29.3	0.3 (+1.2/-1.1)	4.29	0.02 (+0.08/-0.08)	0.80	0.01	-165
Abell 3920	-25.14	0.01 (0.04)	33.0	0.9 (+2.5/-3.0)	6.38	0.08 (+0.21/-0.27)	0.77	0.01	-1296
Abell 4010	-25.89	0.03 (0.25)	223.4	10.6 (+131.0/-69.8)	7.76	0.10 (+0.88/-0.72)	0.65	0.01	-3198
APMC 020	-24.83	0.01 (0.04)	28.8	0.5 (+2.0/-1.7)	4.67	0.04 (+0.15/-0.14)	0.62	0.01	-270
Abell S0084	-26.16	0.04 (0.13)	315.8	24.1 (+98.5/-60.2)	9.53	0.17 (+0.56/-0.41)	0.93	0.01	-3605
Abell S0296 (2000)	-25.14	0.01 (0.01)	29.1	0.2 (+0.9/-0.8)	4.70	0.01 (+0.05/-0.05)	0.68	0.01	-3338
Abell S0296 (1999)	-25.04	0.01 (0.04)	25.9	0.3 (+1.8/-1.5)	4.54	0.03 (+0.15/-0.15)	0.65	0.01	-302
Average									-3680

NOTE. — In the last column $\Delta\chi_d^2 \equiv \chi_{d,sersic}^2 - \chi_{d,deVaucouleurs}^2$. For clusters observed during multiple years, the average and ensemble values are computed using only the 2000 data. Parameter uncertainties corresponding to the 1σ sky level uncertainties are given in parentheses. As in Table 2, the absolute magnitudes are not corrected for extinction or k-dimming. These absolute magnitudes are total magnitudes that include extrapolation beyond $r = 300$ kpc.

TABLE 4
2-DEV PARAMETERS

Cluster	M_{total}	$\sigma_{M_{total}}$	$ \Delta\theta $	$\sigma_{ \Delta\theta }$	M	σ_M	r_e	σ_{r_e}	b/a	$\sigma_{b/a}$	$\Delta\chi_d^2$	$\Delta\chi_s^2$
Abell 0122	-25.66	$^{+0.06}_{-0.06}$	76.5	1.1 (0.5)	-25.56	$0.01^{+0.06}_{-0.06}$	107.9	$2.9^{+9.3}_{-2.3}$	0.53	0.01	-9189	-3156
					-22.97	$0.03^{+0.05}_{-0.05}$	4.7	$0.1^{+0.2}_{-0.2}$	0.63	0.01		
Abell 1651	-25.84	$^{+0.17}_{-0.27}$	9.2	1.3 (0.5)	-24.95	$0.07^{+0.48}_{-0.33}$	477.2	$53.1^{+239.1}_{-130.5}$	0.27	0.01	-328	-289
					-25.21	$0.01^{+0.00}_{-0.00}$	48.2	$0.5^{+0.2}_{-0.2}$	0.78	0.01		
Abell 2376	-23.97	$^{+0.03}_{-0.04}$	68.5	13.2 (5.5)	-23.87	$0.01^{+0.02}_{-0.02}$	18.4	$0.6^{+2.0}_{-1.0}$	0.83	0.01	-2197	-123
					-21.33	$0.08^{+0.09}_{-0.09}$	1.0	$0.1^{+0.2}_{-0.2}$	0.89	0.04		
Abell 2400	-25.17	$^{+0.18}_{-0.32}$	10.0	1.5 (2.5)	-24.61	$0.04^{+0.19}_{-0.44}$	184.6	$44.9^{+169.7}_{-75.2}$	0.41	0.02	-339	-144
					-24.19	$0.08^{+0.17}_{-0.11}$	20.4	$1.0^{+0.8}_{-1.4}$	0.67	0.01		
Abell 2401	-24.62	$^{+0.03}_{-0.03}$	24.4	3.2 (0.4)	-24.48	$0.01^{+0.02}_{-0.02}$	27.6	$0.4^{+1.4}_{-1.9}$	0.88	0.01	-15350	-939
					-22.30	$0.03^{+0.10}_{-0.12}$	1.8	$0.1^{+0.2}_{-0.2}$	0.87	0.01		
Abell 2405	-23.91	$^{+0.17}_{-0.28}$	43.2	2.5 (0.3)	-23.38	$0.02^{+0.25}_{-0.40}$	93.9	$4.7^{+67.3}_{-33.5}$	0.81	0.01	-7687	-1912
					-22.89	$0.01^{+0.06}_{-0.05}$	3.8	$0.1^{+0.2}_{-0.2}$	0.83	0.01		
Abell 2571	-25.42	$^{+0.15}_{-0.19}$	83.6	0.8 (0.5)	-25.11	$0.01^{+0.17}_{-0.22}$	107.7	$5.0^{+43.5}_{-27.9}$	0.52	0.01	-7247	-2667
					-23.89	$0.02^{+0.08}_{-0.09}$	5.4	$0.1^{+0.4}_{-0.4}$	0.68	0.01		
Abell 2721 (2000)	-25.20	$^{+0.02}_{-0.02}$	1.1	1.3 (0.4)	-25.02	$0.03^{+0.04}_{-0.04}$	47.9	$0.8^{+1.8}_{-1.3}$	0.43	0.01	-810	-725
					-23.14	$0.14^{+0.08}_{-0.08}$	18.1	$1.6^{+1.2}_{-1.1}$	0.44	0.01		
Abell 2721 (1999)	-25.19	$^{+0.03}_{-0.04}$	9.7	1.4 (0.5)	-25.04	$0.04^{+0.06}_{-0.06}$	45.8	$0.9^{+2.7}_{-2.7}$	0.43	0.01	-391	-372
					-22.97	$0.21^{+0.09}_{-0.14}$	16.1	$1.9^{+2.0}_{-1.8}$	0.42	0.02		
Abell 2730	-26.14	$^{+0.24}_{-0.30}$	40.3	5.0 (4.6)	-26.00	$0.03^{+0.25}_{-0.25}$	245.9	$13.5^{+121.9}_{-78.4}$	0.72	0.01	-5382	-129
					-23.85	$0.03^{+0.19}_{-0.16}$	8.1	$0.2^{+1.3}_{-1.3}$	0.92	0.01		
Abell 2811	-25.70	$^{+0.22}_{-0.22}$	8.7	3.3 (4.9)	-25.53	$0.03^{+0.22}_{-0.23}$	139.5	$8.6^{+59.7}_{-44.4}$	0.49	0.01	-3556	-204
					-23.59	$0.03^{+0.22}_{-0.22}$	5.5	$0.2^{+0.8}_{-1.0}$	0.85	0.01		
Abell 2955	-25.31	$^{+0.08}_{-0.08}$	70.0	1.9 (2.2)	-25.22	$0.01^{+0.08}_{-0.08}$	93.5	$2.3^{+11.3}_{-9.8}$	0.57	0.01	-10927	-1820
					-22.61	$0.03^{+0.09}_{-0.08}$	3.4	$0.1^{+0.3}_{-0.3}$	0.79	0.01		
Abell 2969	-25.58	$^{+0.26}_{-0.44}$	55.5	9.4 (28.9)	-25.35	$0.03^{+0.27}_{-0.27}$	232.0	$26.7^{+203.6}_{-83.2}$	0.39	0.01	-841	-450
					-23.80	$0.08^{+0.21}_{-0.18}$	19.7	$0.8^{+3.2}_{-1.7}$	0.93	0.01		
Abell 2984	-25.87	$^{+0.01}_{-0.09}$	64.5	8.0 (5.0)	-25.79	$0.01^{+0.01}_{-0.09}$	202.7	$5.4^{+23.2}_{-2.4}$	0.52	0.01	-11873	-1303
					-23.04	$0.02^{+0.04}_{-0.04}$	6.1	$0.1^{+0.6}_{-0.6}$	0.95	0.01		
Abell 3112	-25.82	$^{+0.07}_{-0.07}$	42.3	15.5 (29.5)	-25.74	$0.01^{+0.06}_{-0.06}$	102.1	$1.7^{+12.4}_{-9.4}$	0.41	0.01	-5666	-2260
					-22.95	$0.04^{+0.16}_{-0.17}$	8.3	$0.2^{+0.9}_{-0.9}$	0.96	0.01		
Abell 3166	-24.73	$^{+0.07}_{-0.08}$	82.4	2.1 (0.1)	-24.65	$0.02^{+0.07}_{-0.08}$	69.2	$2.6^{+8.6}_{-6.4}$	0.61	0.01	-3355	-662
					-21.92	$0.04^{+0.08}_{-0.08}$	1.7	$0.1^{+0.2}_{-0.1}$	0.52	0.03		
Abell 3693	-25.63	$^{+0.18}_{-0.18}$	71.5	5.4 (0.6)	-25.46	$0.05^{+0.20}_{-0.10}$	314.5	$24.4^{+61.5}_{-30.5}$	0.84	0.02	-3713	-1178
					-23.56	$0.02^{+0.10}_{-0.04}$	4.9	$0.1^{+0.5}_{-0.5}$	0.68	0.01		
Abell 3705	-24.38	$^{+0.04}_{-0.08}$	2.5	4.1 (2.6)	-24.27	$0.01^{+0.03}_{-0.00}$	30.8	$1.0^{+10.9}_{-2.6}$	0.93	0.01	-3522	-103
					-21.85	$0.07^{+0.62}_{-0.62}$	2.1	$0.1^{+1.3}_{-1.3}$	0.62	0.02		
Abell 3727	-25.14	$^{+0.17}_{-0.19}$	88.3	7.7 (1.5)	-24.97	$0.05^{+0.19}_{-0.21}$	215.2	$17.1^{+54.6}_{-43.7}$	0.68	0.02	-2953	-458
					-23.07	$0.03^{+0.05}_{-0.04}$	6.1	$0.1^{+0.2}_{-0.2}$	0.95	0.01		
Abell 3809	-24.76	$^{+0.07}_{-0.08}$	4.2	1.4 (0.6)	-23.85	$0.03^{+0.04}_{-0.16}$	126.8	$17.2^{+31.4}_{-22.0}$	0.33	0.02	-1096	-931
					-24.14	$0.03^{+0.02}_{-0.02}$	20.8	$0.4^{+0.1}_{-0.2}$	0.91	0.01		
Abell 3920	-25.08	$^{+0.02}_{-0.04}$	0.5	3.3 (0.4)	-24.80	$0.01^{+0.01}_{-0.01}$	45.6	$3.2^{+4.4}_{-3.2}$	0.85	0.01	-1421	-124
					-23.48	$0.10^{+0.07}_{-0.05}$	5.4	$0.4^{+0.1}_{-0.2}$	0.68	0.01		
Abell 4010	-25.71	$^{+0.21}_{-0.28}$	9.4	3.2 (7.4)	-25.56	$0.02^{+0.19}_{-0.28}$	186.3	$10.7^{+107.4}_{-58.1}$	0.47	0.01	-3579	-381
					-23.52	$0.06^{+0.37}_{-0.37}$	13.7	$0.6^{+2.8}_{-3.0}$	0.88	0.01		
APMC 020	-25.12	$^{+0.15}_{-0.38}$	2.4	1.0 (0.3)	-24.34	$0.04^{+0.25}_{-0.62}$	180.2	$34.4^{+259.1}_{-71.3}$	0.32	0.02	-737	-467
					-24.39	$0.03^{+0.07}_{-0.09}$	17.6	$0.4^{+0.9}_{-0.7}$	0.67	0.01		
Abell S0084	-25.38	$^{+0.03}_{-0.05}$	73.6	3.0 (1.3)	-25.33	$0.01^{+0.03}_{-0.05}$	72.0	$1.6^{+3.4}_{-3.9}$	0.85	0.01	-4027	-422
					-21.94	$0.04^{+0.08}_{-0.10}$	2.0	$0.1^{+0.2}_{-0.2}$	0.66	0.03		
Abell S0296 (2000)	-25.20	$^{+0.02}_{-0.04}$	7.1	0.8 (0.9)	-24.89	$0.01^{+0.02}_{-0.00}$	46.1	$1.2^{+7.5}_{-7.5}$	0.57	0.01	-7429	-4091
					-23.67	$0.05^{+0.10}_{-0.19}$	10.0	$0.3^{+0.9}_{-0.3}$	0.78	0.01		
Abell S0296 (1999)	-25.05	$^{+0.03}_{-0.07}$	24.2	3.2 (4.5)	-24.82	$0.04^{+0.15}_{-0.02}$	33.9	$2.1^{+15.1}_{-3.5}$	0.59	0.01	-693	-390
					-23.25	$0.22^{+0.26}_{-0.72}$	8.6	$0.9^{+3.2}_{-0.6}$	0.69	0.01		
Average											-4718	-1039
Average/dof											-786	-208

NOTE. — In the last two columns $\Delta\chi_d^2 \equiv \chi_{2-deV}^2 - \chi_{de\ Vaucouleurs}^2$ and $\Delta\chi_s^2 \equiv \chi_{2-deV}^2 - \chi_{Sersic}^2$. Parameter uncertainties corresponding to the 1σ sky level uncertainties are given in parentheses. As in Tables 2 and 3, the absolute magnitudes are *not* corrected for extinction or k-dimming. These absolute magnitudes are total magnitudes, which include extrapolation beyond $r = 300$ kpc.

TABLE 5
ABELL 1651 SÉRSIC PARAMETERS

	r_e	n
Gonzalez et al. (2000)	59.6 ± 1.1	4.3 ± 0.2
This work	$65.0^{+6.7}_{-5.6}$	$4.26^{+0.17}_{-0.16}$

TABLE 6
AVERAGE ABSOLUTE MAGNITUDES

Model	M_{Total}	$\sigma_{M_{Total}}$	M_{300}	$\sigma_{M_{300}}$	M_{50}	$\sigma_{M_{50}}$	M_{10}	$\sigma_{M_{10}}$
de Vaucouleurs	-24.60	0.56	-24.56	0.53	-24.20	0.39	-23.14	0.30
Sérsic	-25.43	0.83	-24.93	0.50	-24.26	0.36	-23.11	0.28
2-deV	-25.23	0.59	-24.96	0.47	-24.26	0.35	-23.11	0.29

NOTE. — The average absolute magnitudes and the dispersion in these magnitudes for our BCG sample. The column M_{Total} corresponds to the total absolute magnitudes listed in Tables 2 - 4. The columns M_{300} , M_{50} , and M_{10} correspond to the model magnitudes within circular metric apertures of radii 300, 50, and 10 kpc, respectively. The above table does not include extinction or k-corrections, but both effects are small. Accounting for these factors decreases the dispersions by only 0.01 mag. The impact on the mean absolute magnitude can be approximated by assuming a mean extinction of 0.05 mag and a mean k-correction of 0.07 mag.

TABLE 7
IMPACT OF PSF ON DERIVED 2-DEV PROFILE FOR ABELL 0122

PSF	FWHM('')	$\mu_{e,1}$	$r_{e,1}$	$(b/a)_1$	$\mu_{e,2}$	$r_{e,2}$ (kpc)	$(b/a)_2$	$ \Delta\theta $	$\Delta\chi^2$
Abell 0122	1.38	18.77	5.9	0.63	19.67	147.8	0.53	76.5	—
Abell 2376	1.33	18.83	7.4	0.67	19.74	157.9	0.52	72.6	51.7
Abell 3727	1.37	18.81	6.6	0.63	19.71	152.6	0.52	75.3	82.4
Abell S1096	1.49	18.80	6.6	0.63	19.71	153.8	0.53	73.3	-23.9

NOTE. — $\Delta\chi^2$ is the difference between the χ^2 using this PSF and the χ^2 using the correct PSF for the Abell 0122 field.